Cell Reports
Medicine

Article

Reprogramming T cell-myeloid crosstalk overcomes immune resistance in colorectal cancer

Graphical abstract

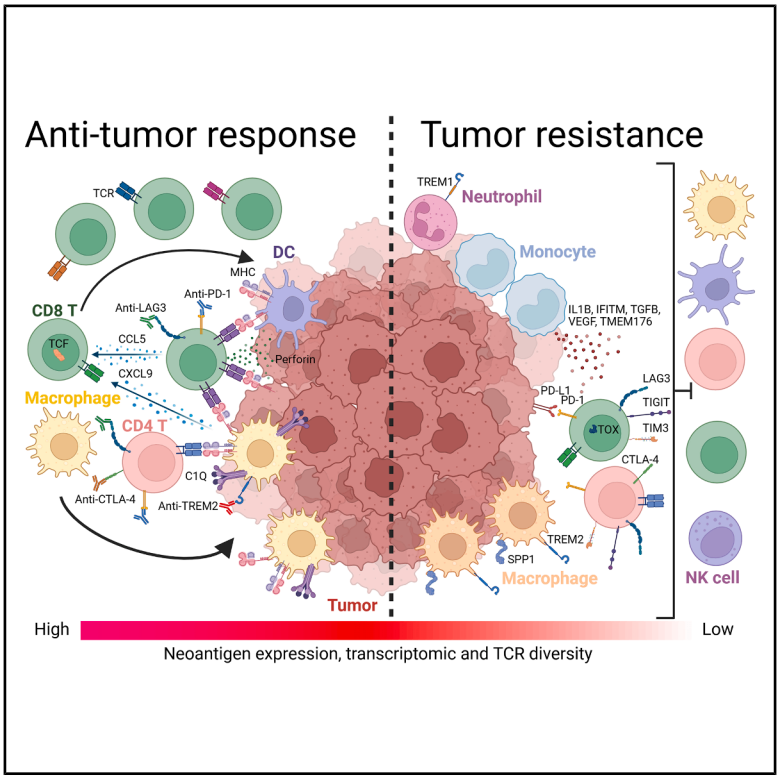

Highlights

- Anti-PD-1 increases TCR diversity and MHCI/II+ macrophage/DC interactions with T cells
- Resistance involves TREM2^{+} macrophages, multiple T cell checkpoints, and IFITM^{+} tumors
- PD-1, LAG3, CTLA-4, and TREM2 blockade prevents MMRd and MMRp tumor progression
- Combination therapy drives macrophage-T cell interactions and immune memory

Authors

Guillaume Mestrallet, Matthew Brown, Natalie Vaninov, ..., Cansu Cimen Bozkus, Robert M. Samstein, Nina Bhardwaj

Correspondence

guillaume.mestrallet@mssm.edu (G.M.), robert.samstein@mountsinai.org (R.M.S.), nina.bhardwaj@mssm.edu (N.B.)

In brief

Mestrallet et al. show that T cell-myeloid interactions determine response to PD-1 blockade in colorectal cancer. Targeting TREM2 macrophages together with LAG3, CTLA4, and PD-1 reprograms the tumor microenvironment and drives antitumor immunity, achieving up to 100% tumor clearance in mismatch repair-deficient and >70% in mismatch repair-proficient models.

Mestrallet et al., 2026, Cell Reports Medicine 7, 102786
May 19, 2026
https://doi.org/10.1016/j.xcrm.2026.102786

CellPress

Cell Reports Medicine

CellPress
OPEN ACCESS

Article

Reprogramming T cell-myeloid crosstalk overcomes immune resistance in colorectal cancer

Guillaume Mestrallet,[1,*] Matthew Brown,[1] Natalie Vaninov,[2] Nam Woo Cho,[3] Leandra Velazquez,[1] Aparna Ananthanarayanan,[1] Matthew Spitzer,[4] Nicolas Vabret,[2] Cansu Cimen Bozkus,[1] Robert M. Samstein,[2,5,*] and Nina Bhardwaj[1,5,6,*]

[1]Division of Hematology and Oncology, Hess Center for Science & Medicine, Tisch Cancer Institute, Icahn School of Medicine at Mount Sinai, New York, NY 10029, USA

[2]The Marc and Jennifer Lipschultz Precision Immunology Institute, Department of Immunology and Immunotherapy, Department of Radiation Oncology, Icahn School of Medicine at Mount Sinai, New York, NY 10029, USA

[3]Department of Radiation Oncology and the Department of Otolaryngology–Head and Neck Surgery, University of California at San Francisco, San Francisco, CA 94143, USA

[4]Department of Otolaryngology–Head and Neck Surgery and the Department of Microbiology and Immunology, University of California at San Francisco, San Francisco, CA 94143, USA

[5]These authors contributed equally

[6]Lead contact

*Correspondence: guillaume.mestrallet@mssm.edu (G.M.), robert.samstein@mountsinai.org (R.M.S.), nina.bhardwaj@mssm.edu (N.B.)

https://doi.org/10.1016/j.xcrm.2026.102786

SUMMARY

Colorectal cancer (CRC) accounts for 10% of cancer cases and is the second leading cause of cancer-related deaths. Although anti-PD-1 therapy improves outcomes, 50% of advanced mismatch repair-deficient (MMRd) and most mismatch repair-proficient (MMRp) CRC cases fail to respond. Using orthotopic and patient-derived CRC models with single-cell and spatial analyses, we show that tumor control during anti-PD-1 treatment associates with colocalization of MHC$^+$ C1Q$^+$ CXCL9$^+$ macrophages and TCF$^+$ PRF1$^+$ T cells. Resistance correlates with increased TIM3, LAG3, TIGIT, and PD-1 expression on T cells and enrichment of TREM2$^+$ macrophages in T cell-excluded regions. A combinatorial blockade targeting TREM2, LAG3, CTLA4, and PD-1 induces up to 100% tumor clearance in MMRd and >70% in MMRp models. This strategy promotes immune memory mediated by interactions among MHC$^+$ macrophages and CD4$^+$/CD8$^+$/TCF$^+$ T cells, while reducing immunosuppressive myeloid infiltration and T cell exhaustion, identifying key cellular programs that overcome immune escape in CRC.

INTRODUCTION

Up to 30% of colorectal, endometrial, and gastric cancers exhibit deficiency in mismatch repair (MMR) protein expression due to germline or epigenetic inactivation, leading to high genomic instability in microsatellite regions (MSI-H).[1–5] As a result, mismatch repair-deficient (MMRd) tumors have an increased frequency of insertions/deletions (indels) that may encode highly immunogenic, novel, shared neoantigens due to common stretches of foreign protein sequences downstream of frameshift mutations at microsatellite regions.[6] Significantly, MMRd cancers become highly infiltrated by T cells expressing PD-1, contributing to the clinical efficacy of anti-PD-1 therapy.[7–10] However, up to 50% of patients with advanced MMRd stage IV and most MMR-proficient (MMRp) colorectal cancer (CRC) cases do not respond to PD-1 blockade, highlighting the need to explore resistance mechanisms limiting the success of checkpoint blockade.[11,12]

Immune resistance can develop during tumor development, namely, intrinsic resistance, or after the initiation of PD-1 blockade,[1] namely, acquired resistance, and is attributed primarily to T cell exhaustion[6,13–16] and a dysregulated tumor microenvironment (TME).[16,17] In human MMRd CRC, an inflammatory hub containing T regulatory cells (Tregs), cancer-associated fibroblasts expressing matrix metalloproteinases, immunosuppressive monocytes, and neutrophils further contribute toward immune evasion, coupled with tumor angiogenesis and tissue remodeling.[16] Following PD-1 blockade in the neoadjuvant setting, MMRd CRC patients who failed to achieve complete response demonstrated reduced baseline intra-tumoral CD8$^+$ T effector memory cells, CD4$^+$ T helper cells, and CD20$^+$ B cells when compared with patients with complete response.[17] Resistance was also accompanied by an increase in tumor infiltration by CD8$^+$ resident memory cells, Tregs, IL1B+ monocytes, and CCL2+ fibroblasts. Other features of the TME that have been associated with resistance include the immunoediting of immunogenic neoantigens and impaired antigen presentation in part due to the loss of beta 2 microglobulin.[1,18] Finally, IFN-induced upregulation of HLA-E, which inhibits CD8$^+$ T cells and natural killer (NK) cells via interaction with the NKG2A/CD94 receptor, has been proposed as an additional resistance mechanism.[19]

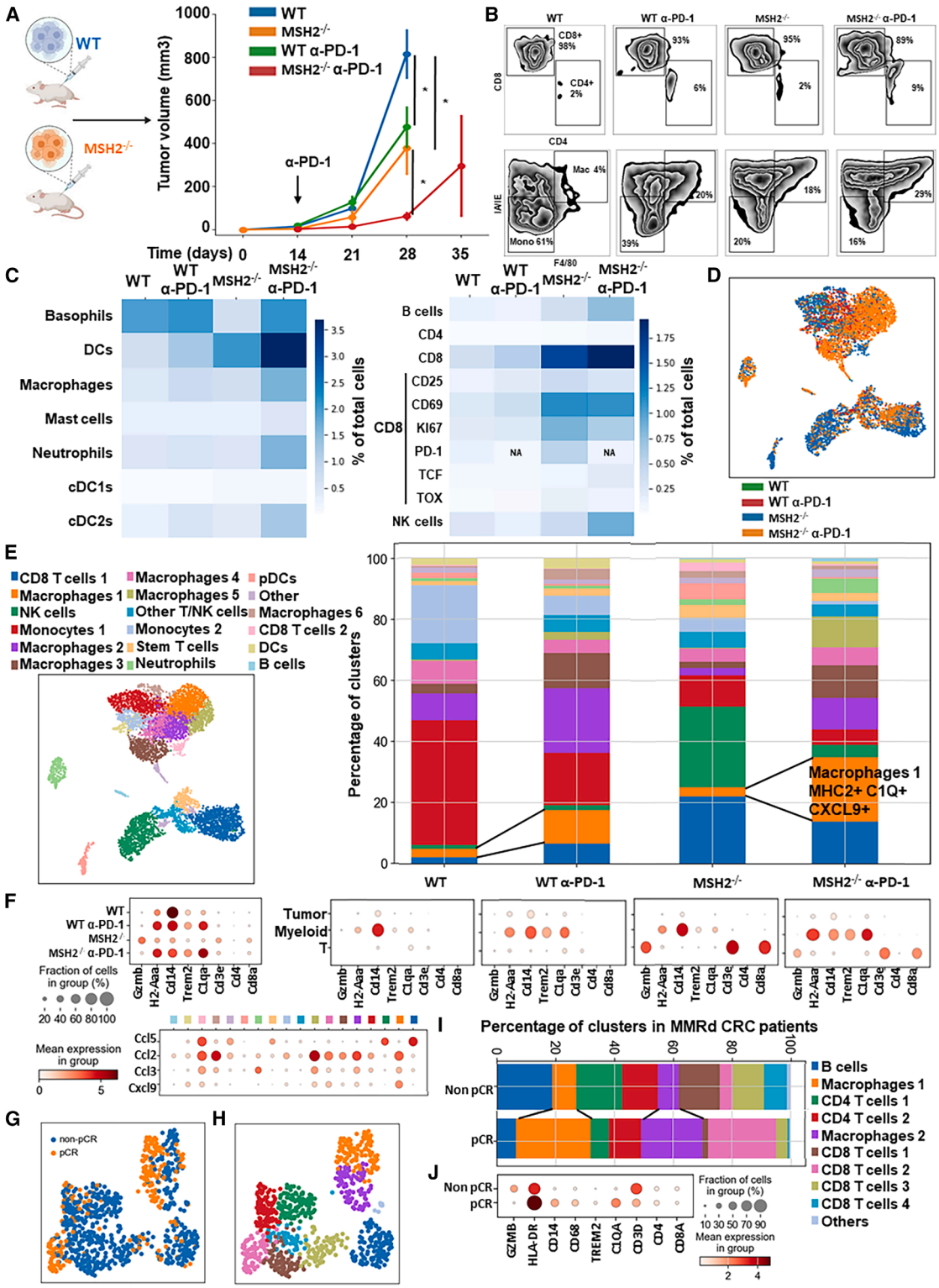

Figure 1. MMRd tumors responding to anti-PD-1 are highly infiltrated by MHC+ C1Q+ macrophages

(A) A total of 200,000 CT26 tumor cells, either deleted or not for MSH2, were allowed to grow subcutaneously for 28 or 35 days in BALB/c mice, with or without anti-PD-1 administered twice a week after 14 days (N = 10 replicates, Mann-Whitney U test, p value <0.05). Validation with 4 other orthotopic models was performed in Figure 4.

(legend continued on next page)

However, the spatiotemporal landscape of immunological determinants supporting treatment response compared with immune checkpoint treatment resistance mechanisms is still not completely defined. This restricts the ability to precisely determine what pathways need to be targeted in order to overcome immune resistance in MMRd tumors and generate robust immune memory.

In this study, we employed spatial and single-cell transcriptomics, spectral flow cytometry, machine learning, and imaging techniques in multiple murine tumor models along with murine and human MMRd CRC spheroid cultures to define pertinent immune resistance pathways. We uncovered evidence suggesting that targeting multiple checkpoints and macrophages simultaneously overcomes resistance in MMRd and MMRp tumors and that TCF+ T cells and MHC+ macrophages orchestrate this response.

RESULTS

MMRd tumors responding to anti-PD-1 are highly infiltrated by MHC+ C1Q+ macrophages and CD8$^+$ T cells

To investigate the determinants of immune response and resistance within MMRd tumors, we utilized a murine colorectal cancer CT26 cell line, in which MSH2, a DNA MMR protein, was either deleted or left intact, thereby modeling MMRd or MMRp tumors, respectively.[6] Cells were injected orthotopically into the caecum or into the flank of BALB/c mice, and after 14 days, once tumors were established, mice were treated with anti-PD-1. As expected, MSH2 knockout (KO) tumor growth was substantially reduced compared with wild-type (WT) tumors after 28 days (Figure 1A). Despite this significant reduction in MSH2 KO tumor growth following anti-PD-1 therapy, tumors persisted and grew gradually until 35 days when mice were euthanized due to tumor burden (Figure 1A). To ensure that the observed differences in tumor sizes *in vivo* between MSH2 KO and WT tumors were not due to different growth rates of the cell lines, we generated spheroids and followed their growth *in vitro*. We observed no difference in spheroid growth based on MSH2 status (Figure S1), confirming that control of tumor growth *in vivo* is likely due to the induction of anti-tumor immunity. Our results confirmed that anti-PD-1 therapy contributed to MMRd tumor control, as seen in human cohorts,[7,8] yet therapy resistance persisted as tumors continued to grow, albeit slower.

To understand which immune subsets are critical in mediating tumor growth control, we investigated immune infiltration within CT26 WT and MSH2 KO tumors, both with and without anti-PD-1 therapy. Using flow cytometry, we observed that both 14 and 28 days after inoculation, MSH2 KO tumors were infiltrated by more immune cells compared with WT tumors (12% vs. 6% after 28 days, p value <0.05) (Figure S2A). Compared with WT tumors, MSH2 KO tumors had increased infiltration by dendritic cells (DCs) and CD4$^+$ T cells at day 14, followed by enrichment of activated proliferating CD8$^+$ T cells at day 28, including PD-1+ CD8$^+$ T cells (Figures 1B and 1C; Figure S2A). MSH2 KO tumors also had greater numbers of NK cells, T cells, B cells, DCs, macrophages, and neutrophils compared with the poorly infiltrated WT tumors (Figure 1C). We confirmed these results by single-cell RNA ssequencing (scRNA-seq) (Figures 1D and 1E; Figure S3). Post-anti-PD-1 therapy, there was a decrease in monocytes and an increase in macrophages, T cells, CD8$^+$ T cell subsets expressing TCF, a marker of stem-like T cells,[20] and neutrophils, particularly notable in MSH2 KO tumors (Figure 1C). These macrophages expressed MHCII; C1Q, a protein that initiates the classical complement pathway of the complement system[21]; CXCL9, a cytokine that attracts CD8$^+$ cytotoxic T cells[22]; and also TREM2, a marker of resistance[23–26] (Figure 1F; Figure S3). Overall, the delayed tumor growth by MSH2 KO tumors, especially following PD-1 blockade, correlates with an increased immune infiltration composed of T cells, including activated CD8$^+$ T cell subsets expressing TCF, DCs, neutrophils, and MHC+ C1Q+ CXCL9+ macrophages.

Last, we compared our observations in murine tumor models with those in human patients. To do so, we conducted retrospective analyses on human COAD and UCEC MMRd cohorts using CIBERSORT data available on The Cancer Genome Atlas (Figure S4A) and the CRI iAtlas (Figures S4B and S4C). Remarkably, the extensive MMRd tumor immune cell infiltration observed in mice (Figures 1C and 1D) was also observed in humans (Figure S4), with notable emphasis on Th2 and CD8$^+$ T cells. Furthermore, we conducted a reanalysis of baseline (e.g., prior to therapy) human MMRd CRC scRNA-seq patient data, focused on patients who either achieved a complete response or did not completely respond to anti-PD-1 therapy, with examination of underlying immune profiles (Figures 1G and 1H; Figure S5).[17] Human MMRd CRC patients who responded to anti-PD-1 therapy had greater infiltration of macrophages expressing C1Q and MHCII (Figures 1I and 1J; Figure S5), mirroring our observations in the mouse model.

Response to anti-PD-1 and infiltration by stem-like T cells correlates with a high tumor mutational load

We next investigated which underlying mechanisms might lead to high immune cell infiltration in MMRd tumors in their response to anti-PD-1. We first explored whether this immune cell increase might be attributable to or correlated with an increased presence in lymph nodes and spleen. We quantified immune cell

(B and C) Quantification of differential lymphocyte infiltration expression according to the MSI status and ICB through spectral flow cytometry at day 28 (N = 6 replicates, Mann-Whitney U test, p value <0.05). Only significant results are shown.
(D) scRNA-seq UMAP of immune cells in CT26 WT and MSH2 KO tumors with or without anti-PD-1 therapy (N = 3 replicates per condition).
(E) UMAP of immune clusters subsequent to Leiden clustering by scanpy. Percentage of cells in each immune cluster.
(F) Gene expression within each immune cluster.
(G–J) We reanalyzed human MMRd CRC patient data previously published,[17] focusing on patients who responded or did not respond to anti-PD-1 therapy alone, and the underlying T cell and macrophage profiles. (N = 9 patients). (G) scRNA-seq UMAP of immune cells in patients who responded (pathological complete response, pCR) or did not respond (non-pCR) to anti-PD-1 therapy. (H) UMAP of immune clusters subsequent to Leiden clustering by scanpy. (I) Percentage of cells in each immune cluster. (J) Gene expression within each immune cluster.

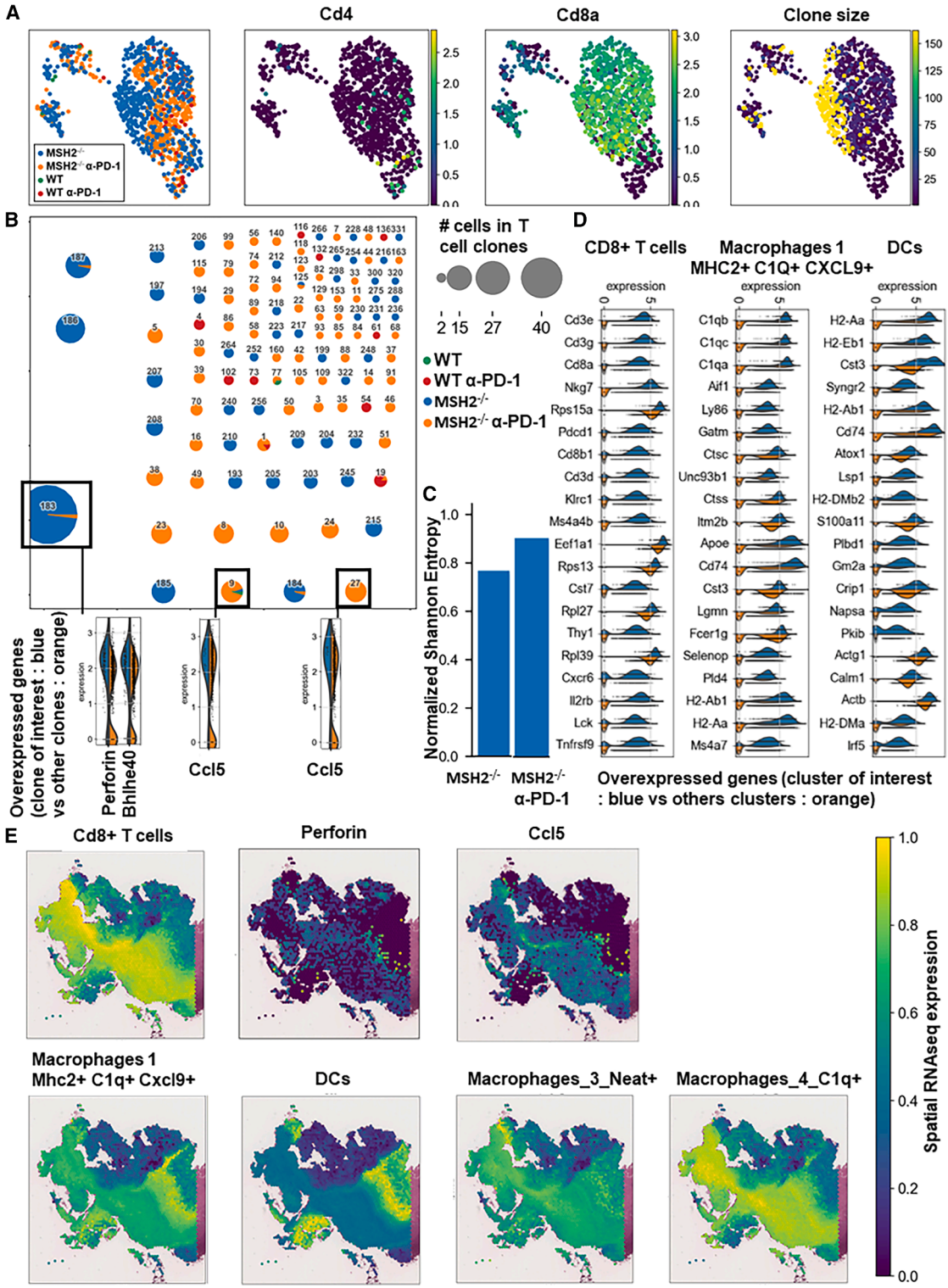

Figure 2. A high diversity of CCL5+ PRF1+ T cell clones, DCs, and MHC+ C1Q+ macrophages colocalize in MMRd tumors responding to anti-PD-1

A total of 200,000 CT26 tumor cells, either deleted or not for MSH2, were allowed to grow for 28 or 35 days in BALB/c mice, with or without anti-PD-1 administered twice a week after 14 days (N = 10 replicates, Mann-Whitney U Test, p value <0.05).

(legend continued on next page)

distribution in the spleen and draining lymph nodes 28 days after tumor injection using spectral flow cytometry. Notably, we observed a higher presence of macrophages and neutrophils in the draining lymph nodes of mice injected with MSH2 KO tumors compared with WT tumors after 28 days (Figure S2E). Following anti-PD-1 therapy, a surge in TCF+ CD4$^+$ and TCF+ CD8$^+$ T cells, DCs, neutrophils, and macrophages was also evident in the spleen of mice injected with MSH2 KO tumors after 28 days (Figure S6C). Moreover, there was an elevated percentage of TCF+ CD4$^+$ and TCF+ CD8$^+$ T cells in the lymph nodes (Figure S6D). In summary, the increased infiltration of TCF+ T cells and myeloid cells into MSH2 KO tumors following PD-1 blockade correlates with increased presence of these cells in both spleen and lymph nodes.

We also investigated whether the high burden and the landscape of mutations in MMRd tumors shape the immune milieu within the TME leading to the elevated TCF+ T cell infiltration. To this end, we utilized different CT26 MSH2 KO cell lines, with high and low mutation loads, respectively, as determined by whole-exome sequencing (WES) (Figure S7). Notably, these different MSH2 KO cell lines displayed differential response to PD-1 blockade. We observed that high indel and SNV loads of the tumor before initiating immune checkpoint blockade (ICB) correlated with delayed tumor growth and an increased infiltration by TCF+ T cells (Figure S7). Tumor allele frequencies of frameshift and SNV mutations also decreased following anti-PD-1 therapy, when comparing pre- and post-treatment time points within the same group, suggestive of immunoediting (Figure S7). Overall, high tumor mutational burden correlates with high infiltration by TCF+ T cells and response to anti-PD-1, suggesting that stem-like T cells and high TMB drive the anti-tumor response.

A high diversity of CCL5+ PRF1+ T cell clones, DCs, and MHC+ C1Q+ macrophages colocalize in MMRd tumors responding to anti-PD-1

Next, we investigated if MSH2 KO tumors having high tumor mutational burden and consequently, increased T cell infiltration were marked by changes in T cell clonal diversity. We applied scRNA-seq coupled with TCR profiling to determine the diversity of tumor-infiltrating T cells (Figure 2A; Figures S8A and S8B). There were very few T cells in WT tumors, limiting the analysis for this condition. Only 4 clonotypes were shared between WT and MSH2 KO tumors (clones 9, 1, 19, and 77), while 5 clonotypes were shared in MSH2 KO tumors with or without anti-PD-1 therapy (clones 183, 187, 125, 9, and 184) (Figure 2B). Notably, MSH2 KO tumors were characterized by the strong expansion of 1 clone (183) in the CD8$^+$ PRF1+ cluster, while anti-PD-1 promoted the expansion of multiple clones (Figure 2B; Figures S8C–S8E) (62 clones in MSH2 KO tumors after ICB vs. 46 clones without ICB). Clone 183 was characterized by expression of the human T cell receptor alpha variable (TRAV) genes TRAV16N and TRAV3-3 and by a higher length of CDR3 regions (Figures S8F and S8G). Interestingly, the more abundant clones in MSH2 KO tumors (183 and 187) overexpress BHLHE40, a tissue-specific regulator of murine tissue-resident macrophage proliferation,[27] associated with repressing IL-10 and increasing IFN-γ secretion, also involved in Th1-like cell and CD8$^+$ memory T cell responses to CD40 agonist immunotherapy in CRC.[28] These clones also overexpressed PRF1, the gene allowing the production of perforin and enabling cytolytic activity of the T cells, suggesting that they are able to target the tumor cells (Figure 2B). The more abundant clones in MSH2 KO tumors following anti-PD-1 therapy (9 and 27) also overexpressed CCL5, a cytokine recruiting various immune cells such as T cells, eosinophils, basophils, monocytes, NK cells, and DCs[29] (Figure 2B; Figure S8H). Overall, recognition of MSH2 KO tumors is characterized by specific TCRs expressed by CD8$^+$ T cells, and anti-PD-1 increased the diversity of the T cell clonal response (Figure 2C), releasing CCL5 and BHLHE40 that may attract other antigen-presenting cells and promote macrophage proliferation, respectively.

Subsequently, we investigated these mechanisms of cooperation between T cells and myeloid cells in the TME *in situ* using spatial transcriptomics. Through the application of scRNA-seq clustering to spatial tumor samples, we observed that CD8$^+$ T cells, along with macrophage clusters 3 and 4 expressing C1Q and MHCII, co-localize within the tumors (Figure S9). These CD8$^+$ T cells and macrophage clusters are in proximity to DCs and macrophage cluster 1, which display the highest levels of C1Q and MHC expression (Figures 2D and 2E; Figure S9). The main TCR clones, overexpressing PRF1, appeared to be enriched between the T cell-enriched and the T cell-excluded zones, suggesting that they drive the anti-tumor response (Figure S8J). CD8$^+$ T cells and NK expressed high levels of CCL5, a cytokine that attracts T cells, while the macrophage cluster 1 expressed high levels of CXCL9, a cytokine that attracts CD8$^+$ cytotoxic T cells, and MHC molecules (Figure 1F). Collectively, the infiltration of MSH2 KO cells by CD8$^+$ T cells and macrophages expressing C1Q and MHC may account for their superior response to anti-PD-1 therapy when compared with WT tumors. Thus, it is plausible that collaboration between DCs, macrophages and CD8$^+$ T cells play a pivotal role in the anti-PD-1 response. The expression of BHLHE40 by tumor-specific cytolytic T cells may increase the recruitment of macrophages. In turn, these macrophages, together with DCs, may increase

(A) TCRseq paired with scRNAseq UMAP of immune cells in CT26 WT and MSH2 KO tumors with or without anti-PD-1 therapy (N = 3 replicates per condition). UMAP of immune clusters subsequent to Leiden clustering by scanpy and clonal expansion of T cell clones. Each dot is a T cell.
(B) Identification of T cell clones, where each clone is uniquely numbered, and their frequency is demonstrated as a pie chart. The number of cells in each clonotype is indicated by the size of each bubble. Selected gene expression within each main T cell clone is shown at the bottom (clone of interest: blue vs. other clones: orange).
(C) Normalized Shannon entropy according to ICB status.
(D) scRNA-seq data and overexpressed genes in T cells, macrophages, and DCs (cluster of interest: blue vs. others clusters: orange).
(E) Spatial localization of each single-cell immune cluster in MSH2 KO tumors with anti-PD-1 therapy. Neighborhood enrichment and quantification were performed using scanpy and squidpy (Figure S9).

the recruitment of tumor-specific and stem-like TCF+ T cells through antigen presentation by MHC and CXCL9 production. Finally, the expression of CCL5 by tumor-specific and stem-like TCF+ T cells and NK may increase the recruitment of additional T cells.

Immune escape is marked by tumor cell selection and upregulation of IFITM and other immunosuppressive genes by cancer cells

We next aimed to identify immunosuppressive pathways exhibiting resistance to anti-PD-1 therapy through scRNA-seq analysis of tumor cells. MSH2 KO and WT tumor cells clustered distinctly, with only a limited number of clusters shared between these two tumor types (Figures S10C and S10D). MSH2 KO tumors generated a more diverse array of clusters compared with WT tumors (12 main clusters vs. 4, respectively [Figure S10D] [more clusters are present following anti-PD-1 therapy]). Interestingly, anti-PD-1 therapy led to a reduction in the cell count within MSH2 KO cluster 6 and WT cluster 7, suggesting that these clusters may be targeted by immune cells (Figure S10D). Post anti-PD-1 treatment, a surge of cells emerged in MSH2 KO cluster number 8 and WT cluster 1, implying the resistance of these clusters to the therapy (Figures S10D and S10E). Within these resistant clusters, an upregulation of genes such as IFITM2, IFITM3, and TMEM176, regulating inflammasome and epithelial-mesenchymal transition,[30–32] and other resistance-associated genes was detected when juxtaposed with clusters effectively targeted by anti-PD-1 (Figures S10F and S10G). Gene enrichment analysis in these tumor scRNA-seq clusters 1 and 8 indicated that resistance involved pathways similar to the ones that negatively regulate viral entry into host cells (Figure S11). In addition, VEGFB exhibited higher expression in MSH2 KO tumors when contrasted with WT tumors (Figure S10C), a phenomenon corroborated by our findings through Luminex analysis on spheroids (Figure S12C). Overall, tumor cells may escape from immune surveillance by upregulating genes associated with resistance in multiple cancers such as IFITM and TMEM176.

Anti-PD-1 resistance is associated with infiltration of TREM2+ macrophages, IL1B+ TREM1+ monocytes, neutrophils, and T cells expressing multiple inhibitory checkpoints

In addition to utilizing intrinsic immunosuppressive tactics, tumors can alter the immune milieu to drive a pro-tumorigenic inflammation. To explore whether the development of MSH2 KO tumors might be linked to immune checkpoint expression, T cell exhaustion, or myeloid immunosuppressive programs, we quantified PD-1, TIM3, TIGIT, CTLA4, and LAG3 immune checkpoints, as well as their corresponding ligand expression in tumor-infiltrating immune cells using flow cytometry and scRNA-seq. Through scRNA-seq and flow cytometry, we identified high levels of PD-1, TIM3, TIGIT, CTLA4, and LAG3 expression in $CD8^+$ TILs (Figure 3A; Figure S3C). Post-anti-PD-1 therapy, the myeloid-infiltrating cells exhibited elevated expression of checkpoint ligands, particularly notable for LAG3 ligands, and molecules such as TREM2, CSF1R, and IL1B, a myeloid cell cytokine previously associated with resistance in MMRd CRC tumors.[17] Additionally, an increase in infiltrating macrophages was observed (Figure 3A; Figure S3). PD-L1 and TIM3 ligands (LGALS9, PTDSS1, CEACAM1, and HMGB1) were identified on macrophages, DCs, and tumor cells. TIGIT ligands (PVR, NECTIN2, and NECTIN3) were predominantly expressed on tumor cells, while LAG3 ligands (H2-AB1, H2-AA, and H2-EB1) were mainly expressed on macrophages and DCs. Notably, TREM2 and CSF1R showed prevalent expression in macrophages, IFITM2 and IFITM3 in monocytes, and IL1B in neutrophils and monocytes. Hence, overexpression of immunosuppressive molecules by myeloid cells and checkpoint expression by T cells could potentially trigger ICB resistance to anti-PD-1 (Figure 3A). Using spectral flow cytometry, we verified an increase in $CD8^+$ T cells expressing PD-1, TIM3, and TIGIT in MSH2 KO tumors when compared with WT (Figure 3B). MSH2 KO tumors displayed a higher presence of exhausted PD-1+ TCF− TIM3+ T cells (TEX) (Figure 3B; Figure S2A). Notably, the elevated PD-1 expression on $CD8^+$ T cells might elucidate the efficacy of anti-PD-1 therapy in MMRd patients. After 28 days, we noted an escalation in $CD8^+$ T cells expressing TIM3 and TIGIT in MSH2 KO tumors treated with anti-PD-1 compared with untreated MSH2 KO and WT tumors (Figure 3B). Furthermore, an increase in neutrophil, macrophage, and cDC2 infiltration was observed in MSH2 KO tumors following anti-PD-1 treatment (Figure 1C). In MSH2 KO tumors treated with anti-PD-1, the spleen and lymph nodes also exhibited an increased presence of $CD8^+$ T cells expressing LAG3, TIGIT, TIM3, and myeloid cells (Figure 3C; Figure S6D). Overall, the immune resistance observed in MMRd tumors after anti-PD-1 treatment might be induced by the expression of other immune checkpoints like TIM3, LAG3, CTLA4, and TIGIT, as well as the expression of TREM2, CSF1R, IFITM, and IL1B by myeloid cells. These resistance programs appear to involve the increased presence of these cells in the spleen and their recruitment from the lymph nodes.

Our next objective was to determine if the resistance to anti-PD-1 involving multiple checkpoints on TILs depends on interactions with the TME or is mediated by a direct effect of PD-1 blockade on immune cells recruited to the tumor. To achieve this, we constructed tumor models with no non-tumor elements of the TME, which are CT26 and B16F10 spheroids comprising MSH2 KO or WT cells, and co-cultured them with naive splenic cells along with anti-PD-1 treatment. Utilizing 3D bi-photon imaging, we observed the infiltration of naive splenic cells into both WT and MSH2 KO CT26 spheroids post anti-PD-1 administration (Figure S12A). These findings were corroborated by our flow cytometry analysis (Figures S12B and S12D). Upon the supplementation of naive splenic cells with anti-PD-1 or anti-CTLA4, we noticed an escalation in $CD8^+$ T cells expressing CD25, CD69, Ki67, TIM3, and TCF, accompanied by a decline in Tregs (Figure S12B). The upregulation of other checkpoints on $CD8^+$ T cells following ICB, such as LAG3 and TIM3, was also observed in the B16F10 model (Figure S12D). Consequently, the immune resistance of MMRd tumors following ICB appears to involve the early upregulation of other immune checkpoints, such as TIM3 and LAG3, due to PD-1 blockade direct effect on immune cells, and is not necessarily dependent on the non-tumor elements of the TME.

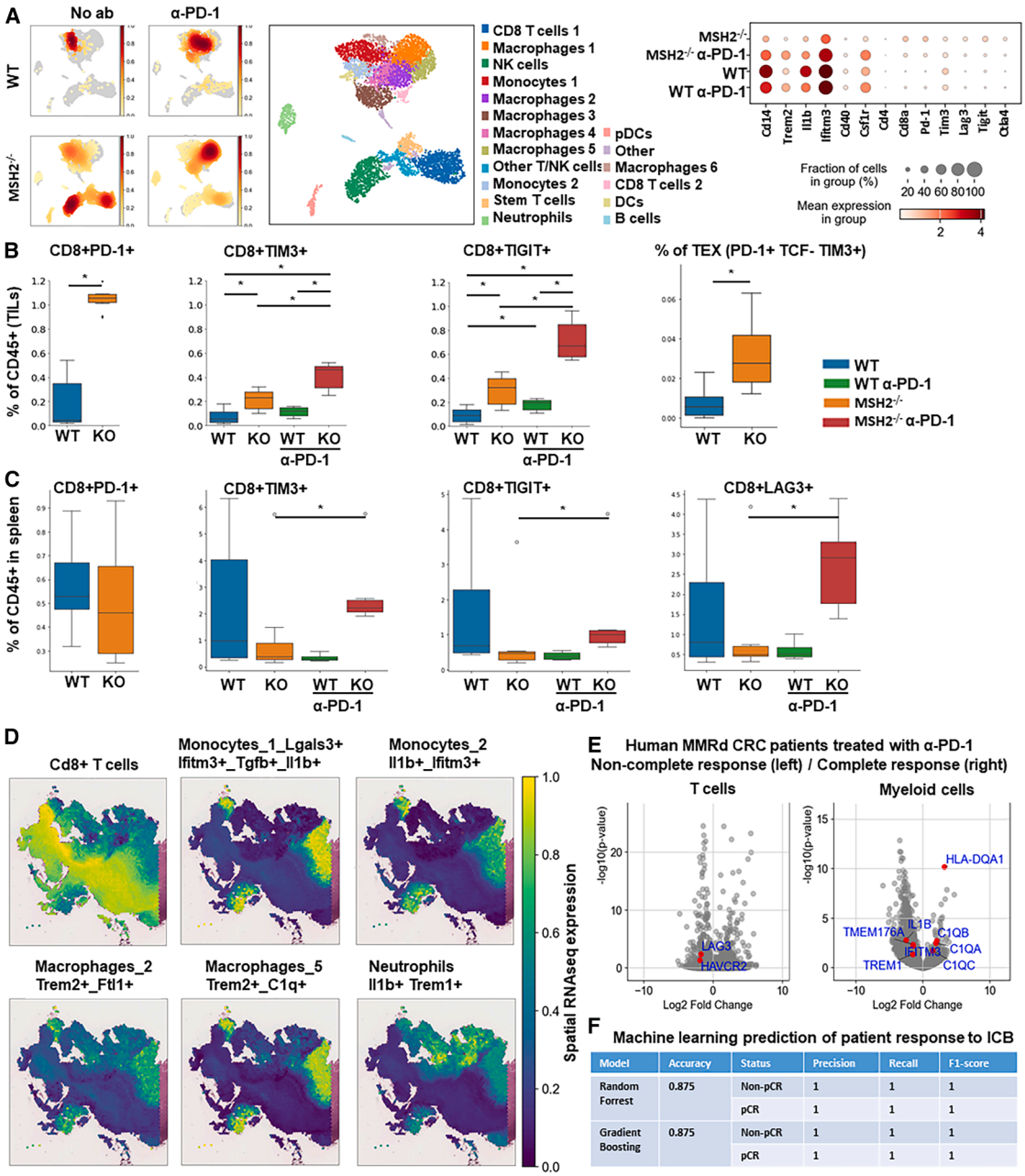

Model	Accuracy	Status	Precision	Recall	F1-score
Random Forrest	0.875	Non-pCR	1	1	1
		pCR	1	1	1
Gradient Boosting	0.875	Non-pCR	1	1	1
		pCR	1	1	1

Figure 3. Immunosuppressive myeloid cells, along with the expression of multiple checkpoints, characterize tumor resistance

(A) scRNA-seq UMAP of immune cells was generated, following the exclusion of tumor cells, in both CT26 WT and MSH2 KO tumors, with and without anti-PD-1 therapy. The distribution of cells and immune genes in each tumor cluster is depicted (N = 3 replicates per condition).

(B and C) The quantification of differential immune checkpoint and lymphocyte infiltration expression in tumors (B) and spleens (C), contingent on the MSI status and ICB, is shown through flow cytometry after 28 days. N = 6 replicates, Mann-Whitney U test, p value <0.05. Data are represented as mean ± SEM.

(D) Spatial localization of each single-cell immune cluster in MSH2 KO tumors with anti-PD-1 therapy. The CD8 panel is the same as in Figure 2E.

(E) A reanalysis of previously published human MMRd CRC patient data[17] has been conducted, focusing on patients with complete or incomplete responses to anti-PD-1 therapy alone and scrutinizing the underlying T cell and macrophage profiles. Gene expression within each immune cluster (N = 9 patients).

(F) RandomForestClassifier and Gradient Boosting algorithms trained on a scRNA-seq dataset[17] (N = 10 MMRd CRC patients). Accuracy = correct predictions/total number of predictions. Precision = correct predictions of a class/all positive true-positive and false-positive predictions. Recall (sensitivity) = correct true-positive predictions of a class/actual instances of the class. F1-score = harmonic mean of precision and recall.

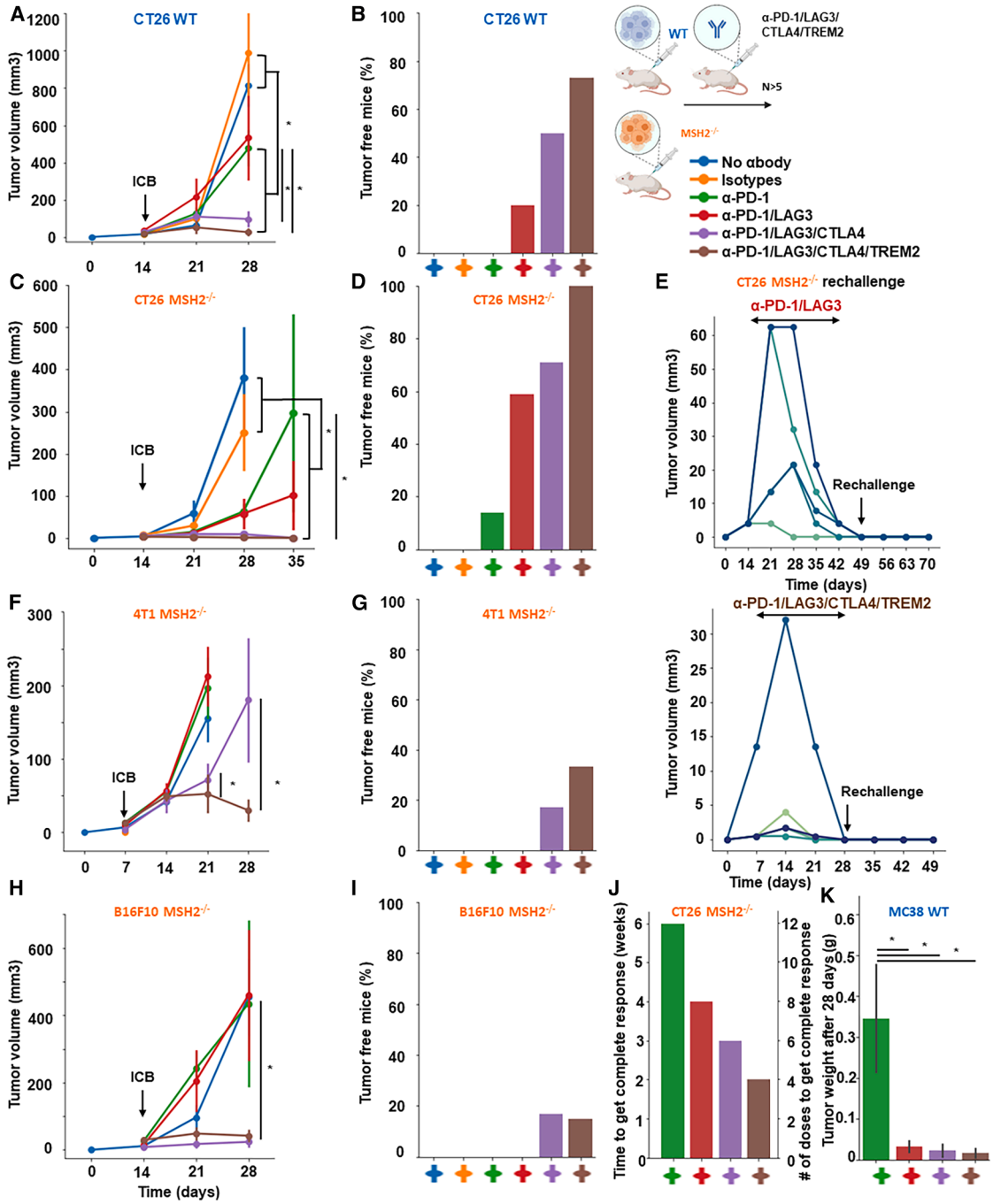

Figure 4. Combination of TREM2, LAG3, CTLA4 and PD-1 blockade eliminates both MMRd and MMRp tumors and elicits robust immune memory

(A, C, F, and H) Tumor volume (mean) *in vivo* over time of CT26 (in the caecum or subcutaneous), B16F10 (subcutaneous), and 4T1 (fat pad) WT and MSH2 KO cells (200,000 cells/tumor) in the absence or presence of anti-PD-1, anti-LAG3, anti-TREM2, or anti CTLA4 (100 μg twice a week after 14 days) therapy (in mm^3). $N = 5–20$ per arm. Mann-Whitney U test, p value < 0.05. Data are represented as mean ± SEM. Detailed results for each single agent or combinations are shown in Table S1 and Figures S14, S15A, S15C, S15F, and S15H.

(B, D, G, and I) Complete response of CT26, B16F10, and 4T1 WT and MSH2 KO tumors after ICB combinations (%).

(legend continued on next page)

Resistance to anti-PD-1 correlates with tumor infiltration by immunosuppressive myeloid cells in T cell-excluded zones

To investigate if there were immunosuppressive mechanisms involving interactions between T cells and myeloid cells in the context of the TME, we applied scRNA-seq clustering to spatial samples. We noted the co-localization of NK cells and monocytes expressing elevated IFITM, LGALS3, TGFB, and IL1B, alongside macrophages in clusters 2, 5, and 6, showcasing heightened TREM2 and IFITM levels in all conditions. These clusters were found within the tumor core, notably within zones marked by the exclusion of CD8 T cells (Figures 3A and 3D; Figures S3 and S9). Neutrophils with elevated IL1B and TREM1 levels were also identified in areas marked by $CD8^+$ T cell exclusion after anti-PD-1 therapy (Figures 3A and 3D; Figures S3 and S9). Immunosuppressive macrophages clusters 2, 5, and 6; monocytes; and neutrophils express high levels of VEGF and IL1RN, which are cytokines that promote Tregs and limit inflammation through competition with IL1, respectively (Figure S3D). Collectively, resistance in WT tumors appears to be characterized by the infiltration of monocytes and the expression of immunosuppressive molecules like IFITM, LGALS3, TGFB, IL1B, VEGF, and IL1RN. Conversely, resistance in MSH2 KO tumors could potentially stem from immunosuppressive macrophages expressing TREM2, VEGF, and IL1RN, TREM1+ neutrophils producing IL1B, and the presence of multiple T cell checkpoints, including TIM3 and LAG3.

Finally, we undertook a reanalysis of previously published human MMRd CRC patient data,[17] with a particular emphasis on patients who had a complete response or no response to anti-PD-1 therapy, while scrutinizing the underlying profiles of myeloid and T cells (Figure 3E; Figure S5). Notably, patients with MMRd CRC who did not respond to anti-PD-1 treatment demonstrated an increased presence of myeloid cells expressing elevated levels of IL1B, TREM1, IL1RN, IDO1, IL6, TMEM176, and IFITM (Figure 3E; Figure S5), akin to our observations in the murine model. Furthermore, non-responders also exhibited a higher population of $CD4^+$ and $CD8^+$ T cells displaying elevated levels of TIM3 and LAG3 (Figure 3E; Figure S5), in parallel to our observations in mice. We hypothesized that we could use these scRNA-seq data to predict which patients will resist or respond to ICB. By applying Random Forest and Gradient Boosting machine learning algorithms on these scRNA-seq datasets, divided into training and validation datasets, we correctly predicted the response to ICB for 87.5% of the patients (Figure 3F). By reanalyzing mutational data from 2 other human CRC cohorts, we observed that most of the non-responders were characterized by a Microsatellite Stable (MSS) status.[13,33] By applying machine learning algorithms on these datasets, we predicted ICB response for these patients (Figure S13). Thus, machine learning can successfully capture the complexity of an individual patient profile to correctly predict the response. Overall, these results imply that targeting myeloid subsets and employing multiple checkpoint blockade strategies may help overcome resistance to anti-PD-1 therapy in CRC.

Combination of TREM2, LAG3, CTLA4, and PD-1 blockade eliminates both MMRd and MMRp tumors

Based on our observations, we next investigated the impact of targeting multiple T cell checkpoints on tumor growth by using anti-TIM3, anti-TIGIT, anti-LAG3, or anti-CTLA4, alone or in combination with anti-PD-1. We injected CT26, 4T1, and B16F10 MMRd or MMRp cell lines into mice and used anti-TIM3, -TIGIT, -LAG3, and -CTLA4 alone or in combination with anti-PD-1, 14 days following tumor inoculation. The *in vivo* tumor volume was assessed and compared, taking into consideration both immune checkpoint blockade and MSH2 status (Figures 4A, 4C, 4F, and 4H). Detailed results for each single agent or combinations are shown in Table S1 and Figures S14, S15A, S15C, S15F, and S15H. Importantly, upon the administration of anti-TIM3, -TIGIT, -LAG3, or anti-PD-1, we observed suppression in the subcutaneous growth of MSH2 KO CT26 tumors after 28 days (Figure 4C; Figure S15C).

This effect was further amplified with the utilization of anti-TIM3, -TIGIT, -LAG3, and -CTLA4 in combination with anti-PD-1 after 35 days, with the most favorable outcomes seen for the anti-PD-1/LAG3/CTLA4 combination. These combinations led to an increase in complete responses and even tumor elimination (Figures 4C and 4D, Table S1; Figures S15C and S15D). WT tumors exhibited responsiveness to the anti-PD-1/LAG3, anti-PD-1/TIGIT, and most effectively to anti-PD-1/LAG3/CTLA4 combinations (Figures 4A and 4B; Figures S15A and S15B). In the context of MMRd CRC tumors, we observed complete responses of 25%, 12%, 59%, and 71% for anti-PD-1/TIM3, anti-PD-1/TIGIT, anti-PD-1/LAG3, and anti-PD-1/LAG3/CTLA4, respectively (Figure 4D; Figure S15D). On the other hand, for WT CRC tumors, complete responses were observed in 0%, 10%, 20%, and 50% cases for anti-PD-1/TIM3, anti-PD-1/TIGIT, anti-PD-1/LAG3, and anti-PD-1/LAG3/CTLA4, respectively (Figure 4B; Figure S15B). Incorporating the 4T1 and B16F10 orthotopic models, we also noted a restriction in MMRd tumor growth upon administration of anti-PD-1/CTLA4/LAG3 (Figures 4F and 4H; Figures S15F and S15H). Interestingly, to observe a complete response in the 4T1 and B16F10 orthotopic models that do not respond to PD-1 blockade alone, it was essential to include anti-CTLA4 alongside the combinations identified for the CT26 model (Figures 4G and 4I; Figures S15G and S15I).

We also investigated the impact of targeting myeloid cell checkpoints or cancer cell programs together with T cell checkpoints on tumor growth by using anti-IL1B, anti-TREM2, or anti-IFITM, alone or in combination with anti-PD-1/CTLA4/LAG3. Targeting TREM2 or IFITM limited MMRd tumor growth (Figure 4C; Figure S15C), but blocking IL1B was not beneficial. Blocking

(E) After CT26 MSH2 KO tumor elimination following anti-PD-1 + anti-LAG3 ± anti-TREM2 therapy, treatment was stopped and a second tumor was inoculated, and its growth was measured for 3 weeks. $N = 5$. Each curve is for an individual mouse.

(J) Time and number of antibody doses needed to observe complete response and CT26 MSH2 KO tumor elimination.

(K) Tumor weight (mean in g) *in vivo* over time of MC38 cells (200,000 cells/tumor in the caecum) in the absence or presence of anti-PD-1, anti-LAG3, anti-TREM2, or anti CTLA4 therapy (100 μg twice a week after 14 days). $N = 5$ per arm. Mann-Whitney U test, p value < 0.05.

TREM2 in addition to T cell checkpoints further limited tumor growth in MMRd and MMRp models (Figures 4B, 4D, 4G, and 4I; Table S1). In the context of MMRd CRC tumors, we observed complete responses of 20%, 50%, and 10% for anti-PD-1/TREM2, anti-PD-1/LAG3/TREM2, and anti-PD-1/IFITM, respectively (Figure 4D; Figure S15D). Notably, the most favorable outcomes were seen for the anti-PD-1/LAG3/CTLA4/TREM2 combination, with complete responses of 100% for MMRd CRC and 73% for MMRp CRC (Figures 4B and 4D; Figure S15). This combination was also efficient in the B16F10 and 4T1 models (Figures 4F–4I; Figure S15). The number of antibody doses and the time needed to achieve complete response and tumor elimination was reduced when using multiple ICBs and anti-TREM2 compared with anti-PD-1 alone (Figure 4J) and less skin lesions were noticed, limiting mouse exposure to potential chronic adverse events. We also validated the superior efficacy of our combinations orthotopically in the caecum for another MMRp model in another genetic background using the MC38 model compared with PD-1 therapy alone by comparing tumor weight after 28 days (Figure 4K). Overall, the combination of TREM2, LAG3, CTLA4, and PD-1 blockade is the most efficient and eliminates both MMRd and MMRp tumors.

Next, we investigated if tumor elimination following multiple checkpoint blockades successfully elicited a memory response and could prevent tumor recurrence. We observed that all mice were effectively protected against a second tumor inoculation subsequent to the elimination of the initial tumor through multiple ICB, suggesting the establishment of potent anti-tumor immune memory mediated by the combination of ICB treatments (Figure 4E). Furthermore, we noted that the proportion of effector memory $CD8^+$ and $CD4^+$ T cells in the spleens and lymph nodes of mice that successfully eradicated an MSH2 KO tumor following anti-PD-1 and anti-LAG3 therapy was higher compared with mice unable to eliminate the tumor (Figure S15J). In conclusion, these findings underscore that targeting multiple immune checkpoints and TREM2 macrophages in MMRd and MMRp tumors not only further curbs tumor growth but also can culminate in complete tumor eradication. The utilization of such ICB and myeloid-targeting combinations holds potential for mitigating immune resistance in both MMRp and MMRd tumors.

Interactions between TCF+, $CD4^+$, and $CD8^+$ T cells, MHC+ macrophages, and neutrophils orchestrate the complete response to targeted checkpoint/myeloid combinations

We next examined the immune subsets that differentially infiltrate MSH2 KO and WT tumors in mice after anti-TIM3/TIGIT/LAG3, with or without anti-PD-1 therapy (Figures S16A, S17A, and S17E). We compared immune infiltration in tumors based on tumor weight and ICB status (Figure S16A). Notably, we observed weight reduction in MSH2 KO tumors after multiple ICB interventions. Crucially, there was no discernible difference in overall immune infiltration correlated with tumor weight. We detected increased infiltration of $CD8^+$ T cells, particularly those expressing TCF, KI67, PD-1, TIM3, LAG3, and TIGIT, alongside $CD4^+$ T cells, mast cells, macrophages, neutrophils in smaller tumors, coupled with increased MHC expression (Figure S16A). Additionally, anti-LAG3 increased MHCII expression on tumors, reduced myeloid infiltration, and enhanced T cell infiltration. Anti-TIM3 decreased myeloid infiltration and increased $CD4^+$ TCF+ T cell infiltration. Anti-TIGIT increased both $CD4^+$ TCF+ T cell and $CD8^+$ TCF+ T cell infiltration (Figure S17A). By way of scRNA-seq and spatial RNA-seq, we observed that following anti-PD-1 + anti-CTLA4 + anti-LAG3 + anti-TREM2, MSH2 KO tumors were more infiltrated by CD4 T cells, MHC+ macrophages, neutrophils, and TCF+ or ICOS+ T cells and less by SPP1+ macrophages, previously described as immunosuppressive,[34] monocytes, and exhausted T cells compared with untreated or anti-PD-1-treated mice (Figures 5A and 5B; Figure S9). Importantly, when adding anti-TREM2 to PD-1/LAG3 blockade, mice with a decrease in tumor volume had lower infiltration of immunosuppressive macrophages but still enriched in TCF+ PD-1+ T cells and DCs compared with non responders (Figure 5C). Compared with CT26 MSH2 KO tumors, 4T1 MSH2 KO tumors contained more monocytes and neutrophils but less T cells, especially T cells expressing TCF and PD-1, and that may explain their stronger resistance to ICB (Figure S18). By measuring T cell phenotype and MMRd spheroid killing following coculture with MonoMacs from tumor or lymph node (LN) of mice bearing CT26 MSH2 KO tumors treated with anti-PD-1 or anti-PD-1/LAG3/CTLA4/TREM2, we observed an increase in T cell activation and tumor spheroid killing following coculture with MonoMacs from mice treated with anti-PD-1/LAG3/CTLA4/TREM2 (Figure S19). Overall, response to multiple checkpoint and myeloid blockades is driven by both CD4 and CD8 T cells, including T cells expressing TCF, ICOS, PD-1, and KI67, as well as neutrophils and MHC+ macrophages, and MHC expression by tumor cells.

We explored whether this increase in immune infiltration of MSH2 KO tumors following multiple ICB/myeloid targeting therapy might be attributable to an increased immune recruitment from lymph nodes and spleen. To investigate this, we assessed immune distribution through flow cytometry in the spleen and lymph nodes 28 days post-tumor injection and multiple ICB/myeloid targeting therapies according to tumor weight after 28 days (Figures S16B and S16C). We also compared these outcomes in mice that responded (tumor rejection) and those that did not (Figures S17C, S17D, and S17F). Responders to multiple ICBs/myeloid targeting had increased counts of $CD4^+$ T cells; $CD8^+$ T cells, particularly TCF+ T cells; as well as $CD8^+$ T cells expressing KI67, PD-1, DCs, along with diminished mast cells, basophils, and polymorphonuclear myeloid-derived suppressor cells in both the spleen and lymph nodes (Figure 5D; Figures S17C, S17D, and S17F). Blocking IL1B was not beneficial and was associated with a diminution in TCF+ T cells and an increase in Tregs in the spleen (Figure S16F). Thus, the increased infiltration of T cells and especially T cells expressing TCF, PD-1, and KI67 into MSH2 KO tumors following successful multiple checkpoint blockade might be attributed to escalated recruitment from both spleen and lymph nodes.

To explore the effectiveness of ICB combinations in a human context, we conducted experiments using patient-derived MMRd CRC spheroids with immune infiltration and stimulation using anti-PD-1, anti-TIM3, and anti-LAG3. We observed that ICB led to an increased infiltration of TCF+ T cells, along with MHC+ macrophages and neutrophils (Figure 5E; Figure S19).

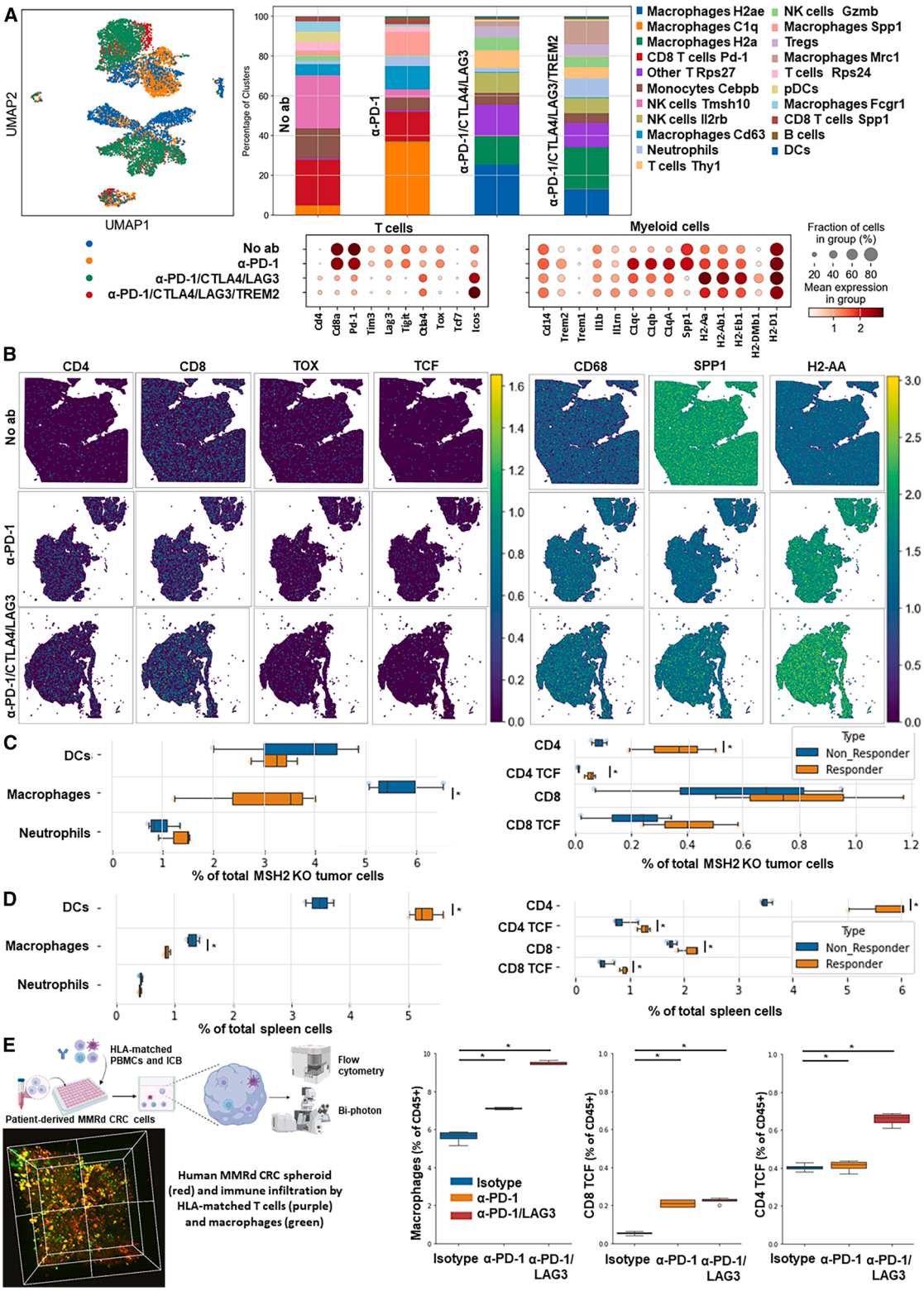

(legend on next page)

Notably, the infiltration of these subsets was further amplified when anti-PD-1 was combined with either anti-TIM3 or anti-LAG3. These findings align with the results obtained from the mouse model (Figures 5A–5C), suggesting that ICB combinations could also prove effective in human contexts and involve TCF+ T cells, both CD4 and CD8 T cells; neutrophils; and MHC+ macrophages.

DISCUSSION

ICB therapy demonstrates a high response rate and durable clinical benefit in patients with MMRd tumors. Our study revealed that the immune response of MMRd CRC tumors is mediated by coordinated myeloid and lymphocyte infiltration, including T cells, DCs, NK cells, and MHC+ C1Q+ macrophages. Additionally, we found that this broad immune response is enhanced following anti-PD-1 therapy in both mouse and human settings. T cells may recognize highly immunogenic shared frameshift-derived neoantigens in MMRd tumors.[13] The observed overexpression of PD-1 in MMRd tumors might explain why they are more responsive to anti-PD-1 therapy.[6–9] Previous research demonstrated the significance of TCF+ T cells in the response to anti-PD-1 in a melanoma model,[20] and our results indicate a similar mechanism in MMRd CRC tumors. Intriguingly, we demonstrated that the response also involves MHC+ C1Q+ CXCL9+ macrophages and DCs that co-localize between T cell exclusion zones and T cell-enriched zones. Notably, this C1Q signature was linked to a poor prognosis in clear-cell renal cell carcinoma,[21] but CXCL9 attracts $CD8^+$ cytotoxic T cells and is associated with better outcomes.[22] These results are in line with recent data from human cohorts that suggest that responsive hypermutated CRCs were enriched in cytotoxic and proliferating PD-1+ CD8 T cells interacting with PDL1+ antigen-presenting macrophages.[33] The remodeling of the infiltrating monocytes and macrophages was observed in other models following ICB.[35] Thus, macrophage remodeling to a more favorable type and the collaboration among DCs, MHC+ C1Q+ macrophages, and $CD8^+$ TCF+ T cells plays a crucial role in the anti-PD-1 response in tumors. This response may be facilitated by an increased presence of these cells by the spleen and their recruitment from the lymph nodes.

Response rates vary, but up to 70% of patients with advanced MMRd tumors do not respond to anti-PD-1 therapy.[1,11,12] We have demonstrated that MMRd tumor resistance involves immunosuppressive tumor and myeloid cells, as well as the expression of multiple checkpoints. Our observations indicate that MMRd tumors possess a higher epithelial cell transcriptomic diversity, maybe due to more mutations, compared with MMRp tumors, and that anti-PD-1 therapy does not effectively target all these tumor clusters. Those MMRd and MMRp clusters that resist anti-PD-1 treatment upregulate IFITM and TMEM176, controlling inflammasome and epithelial-mesenchymal transition, and other genes associated with resistance in multiple cancers.[30–32,36] Furthermore, we have observed that tumors resistant to anti-PD-1 treatment exhibit higher infiltration of TREM2+ macrophages, monocytes, neutrophils, and monocytes expressing IL1B. Previously, high expression of IL1B by monocytes has been associated with resistance in MMRd CRC tumors,[17] as well as TREM2 in multiple models.[23–26] These subsets colocalize in T cell exclusion zones in MMRd and MMRp tumors. Importantly, our data demonstrate that the immune resistance of MMRd tumors can also be attributed to the expression of multiple T cell checkpoints (PD-1, TIM3, LAG3, CTLA4, and TIGIT). This finding aligns with the fact that MMRd polyps are characterized by CTLA-4, LAG3, and PD-L1 expression.[14–16] Other mechanisms of resistance may involve cancer-associated fibroblasts, Tregs, and neutrophils.[16,17,37] Overall, the resistance of MMRp tumors is mediated by monocytes that highly express IFITM, TMEM176B, LGALS3, TGFB, and IL1B. In MMRd tumors, resistance following anti-PD-1 treatment is driven by the expression of TIM3, LAG3, CTLA4, and TIGIT by TILs, as well as tumor clonal selection and the expression of TREM2, CSF1R, IFITM, TMEM176B, and IL1B by myeloid cells. These resistance programs correlate with an increased presence of these immune cells by the spleen and presence in the lymph nodes.

Our data showed that checkpoint receptor and myeloid cell targeting combinations overcome MMRp and MMRd tumor resistance. Following anti-TIM3, anti-TIGIT, anti-LAG3, anti-TREM2, or anti-PD-1 treatment, we observed a limitation in MSH2 KO CRC tumor growth. This effect was amplified when using combinations of anti-PD-1 with anti-TIM3/TIGIT/LAG3/TREM2/IFITM/CTLA4. The most robust responses were

Figure 5. TCF+ T cells, $CD4^+$ and $CD8^+$ T cells, neutrophils, and MHC+ macrophages orchestrate the response to targeted checkpoint/myeloid combinations

CT26 tumors deleted for MSH2 are growing for 28 days in BALB/c mice.

(A) scRNA-seq UMAP of immune cells in CT26 MSH2 KO tumors with or without anti-PD-1/CTLA4/LAG3/TREM2 therapy. UMAP of immune clusters subsequent to Leiden clustering by scanpy. Percentage of cells in each immune cluster and gene expression within each immune cluster ($N = 3$ replicates per condition).

(B) Spatial RNA-seq localization of each single-cell immune cluster in MSH2 KO tumors following ICB. Neighborhood enrichment and quantification were performed using scanpy and squidpy (Figure S9).

(C) Quantification by flow cytometry of differential immune checkpoint and lymphocyte infiltration expression according to response to PD-1/LAG3/TREM2 blockade. $N = 8$ replicates, t test, p value < 0.05. Data are represented as mean ± SEM. Mice with a decrease in tumor volume following therapy are considered as responders, while mice with an increase in tumor volume following therapy are considered as non-responders.

(D) Immune composition in spleens and lymph nodes was also measured (flow cytometry). $N = 8$. Mann-Whitney U test, p value < 0.05. Data are represented as mean ± SEM.

(E) Ten thousand MMRd CRC patient-derived cells are growing for 3 days as spheroids and 100,000 peripheral blood mononuclear cells (PBMCs) from 3 donors are activated with IL-15. Then, spheroids and PBMCs are incubated for 3 days. PBMCs were incubated before with anti-PD-1, anti-TIM3, and anti-LAG3 (10 μg/mL). Immune cells are previously labeled by CellTracker (red). Spheroid cell nuclei are labeled with NucBlue (blue). Spheroids were washed to remove non-infiltrating immune cells before analysis. 3D bi-photon imaging and flow cytometry staining of spheroids after dissociation. Quantification of differential immune checkpoint expression and lymphocyte infiltration according to ICB. $N = 4$. Mann-Whitney U test, p value < 0.05. Data are represented as mean ± SEM.

observed for the anti-PD-1/LAG3/CTLA4/TREM2 combination in MMRd and MMRp tumors. Notably, this combination significantly increased the occurrence of complete tumor elimination, reaching up to 100% for MMRd CRC tumors and up to 73% for MMRp CRC tumors. Adding anti-CTLA4 to the combinations identified in the CRC model was necessary to achieve a complete response in breast and melanoma MMRd cancer models, which is consistent with other studies.[37] We observed that all mice that successfully eliminated a first tumor through targeted checkpoint therapy were effectively protected against a second tumor inoculation, indicating the development of effective anti-tumor immune memory, and may limit the risk of neoplasia.[38] Thus, tailored immunotherapies based on the patient's tumor profile hold potential benefits.

By measuring immune infiltration in mouse tumors, spleens, lymph nodes, and human MMRd CRC patient-derived spheroids, we observed that the response to targeted checkpoint blockade involves MHC+ macrophages, both CD4 and CD8 T cells, neutrophils, TCF+ T cells, and memory T cells. This response also correlates with a reduction of T cell exhaustion and infiltration by SPP1+ TREM2+ macrophages. Consistent with our results, T cells expressing TCF have been shown to be a stem-like population that is central to the maintenance of long-term antiviral immunity and responsiveness to immunotherapy in a melanoma model.[20,39] Our results showed that this stem T cell subset is also key in the response to multiple checkpoint blockade, especially in tumors with high indel and SNV loads, together with MHC+ macrophages and neutrophils.

Our findings have multiple implications for cancer immunotherapy. Our results show that strategically targeting TIM3, LAG3, TIGIT, CTLA4, IFITM, TREM2, and PD-1 in MMRd and also MMRp CRC tumors not only further limits tumor growth but also can significantly increase the complete elimination of tumors. Using anti-LAG3 or anti-CTLA4 with anti-PD-1 is promising for MMRd CRC patients[40,41] and other cancers such as melanoma.[42,43] We showed that targeting these 3 checkpoints together and targeting myeloid cells based on the patient's tumor profile could aid in mitigating immune resistance in both MMRp and MMRd tumors. These combinations could be employed alongside other strategies targeting myeloid subsets, including monocytes, neutrophils, and immunosuppressive macrophages.[23,25,44,45] While we have provided comprehensive analyses using orthogonal approaches in both human and mouse settings, it is likely that TCF+ T cells, MHC+ macrophages, and neutrophils are not the sole subsets driving targeted ICB responses in MMRd CRC tumors. Complementary approaches could also focus on γδ T cells, especially in MMRd cancers with MHCI defects[46]; DCs[28,47]; PD-1- and PI3K-γ-expressing myeloid cells[48,49]; the HLA-E and HLA-G molecules[19,34,50–55]; WRN inhibitors[56]; TREM1 myeloid cells[57]; or vaccination.[58]

In conclusion, a combinatorial checkpoint blockade targeting TREM2, LAG3, CTLA4, and PD-1 achieves up to 100% tumor clearance in MMRd CRC and >70% in MMRp CRC models, compared with 0% with anti-PD-1 monotherapy. We provide the description of the immune landscape of the response mediated by this strategy at the single cell and spatial levels. This approach induces durable anti-tumor immune memory, mediated by coordinated interactions among MHC+ macrophages, CD4+/CD8+ T cells, and TCF+ T cells. It also reduced infiltration by immunosuppressive myeloid cells and T cell exhaustion. Together, this study identifies key T cell and macrophage subsets mediating the efficacy of immunotherapy in overcoming immune escape in both MMRd and MMRp CRC settings.

Limitations of the study

Further validation in patients will be required to confirm the translational potential, safety, and therapeutic window of this combinatorial strategy. More experiments may also be performed using immunodeficient mice to confirm the role of the immune system. The interpretation of the C1Q signature remains unclear, as it was upregulated following PD-1 blockade, but downregulated following combination therapy. Based on our data, we believe that macrophages associated with favorable anti-tumor responses are more robustly characterized by the expression of antigen presentation and inflammatory markers such as MHC and CXCL9.

RESOURCE AVAILABILITY

Lead contact

Further information and requests for the resources, data and reagents should be directed to and will be fulfilled by the lead contact, Nina Bhardwaj (nina.bhardwaj@mssm.edu).

Materials availability

This study did not generate new unique reagents.

Data and code availability

1. Data

Data are available on Mendeley: https://data.mendeley.com/datasets/ct2m5rfwvm/1.

We used raw RNA-seq data from The Cancer Genome Atlas (TCGA) presented in two previous works and merged using TCGA identifiers.[13,59] Data reported in this study are tabulated in the main text and supplemental information.

2. Code

This study did not generate custom computer code.
Code is available on GitHub and GoogleColab.
https://github.com/gmestrallet/BasicScRNAseq
https://github.com/gmestrallet/BasicSpatialRNAseq
https://github.com/gmestrallet/IntegratingSpatialAndScRNAseq
https://github.com/gmestrallet/TCRscRNAseqAnalysis.

3. Additional information

Any additional information required to reanalyze the data reported in this work paper is available from the lead contact upon request.

ACKNOWLEDGMENTS

The authors thank all the current and previous members of the Bhardwaj, Samstein, Merad, and Vabret labs for critical comments on the manuscript. The authors also thank the members of the Human Immune Monitoring Center for processing the Luminex, scRNA-seq, and spatial RNA-seq samples and providing the data and the members of the flow cytometry core, the microscopy core, and the pathology core at Mount Sinai Hospital for helpful discussions and training to prepare the experiments. This work was supported in part through the computational and data resources and staff expertise provided by Scientific Computing and Data at the Icahn School of Medicine at Mount Sinai and supported by the Clinical and Translational Science Awards (CTSA) grant

UL1TR004419 from the National Center for Advancing Translational Sciences. Research reported in this publication was also supported by the Office of Research Infrastructure of the National Institutes of Health under award numbers S10OD026880 and S10OD030463. The content is solely the responsibility of the authors and does not necessarily represent the official views of the National Institutes of Health. The results shown here are in part based on data generated by the TCGA Research Network: https://www.cancer.gov/tcga. Funding: National Institute of Health (NIH) Public Health Service Institutional Research Training award AI07647 (M.B.).

AUTHOR CONTRIBUTIONS

G.M., C.C.B., R.M.S., and N.B. conceptualized the project. G.M. performed the *in vivo* and *in vitro* experiments. G.M. performed the analysis of the genetic, flow cytometry, and microscopy data. M.B. helped with WES analysis. N. Vaninov helped with the *in vivo* orthotopic experiments for the 4T1 model. L.V. and A.A. provided human blood samples and other reagents. N.W.C. and M.S. provided the polyclonal CT26 MMRd cell line and financed WES. G.M. wrote the manuscript. G.M., N. Vabret, C.C.B., R.M.S., and N.B. revised the manuscript.

DECLARATION OF INTERESTS

M.B. is a Parker Scholar with the Parker Institute for Cancer Immunotherapy. R.M.S. is a co-inventor on a patent (US11230599/EP4226944A3) filed by MSKCC for using TMB to predict immunotherapy response, licensed to Personal Genome Diagnostics (PGDx). N.B. is an extramural member of the Parker Institute for Cancer Immunotherapy. N.B. received research support from Harbour Biomed Sciences, stock option from BreakBio, serves as Advisor/Board Member at Curevac, serves as Advisor/Board Member and received stock option from Genotwin and DC Prime, serves as Advisor/Board Member and received equity from Cell BioEngines, received hold stocks from Barinthus, serves as consultant and grant recipient at Merck Research Laboratories, received a drug product from Oncovir and serves at scientific advisory board, and received stock options from Aikium.

STAR★METHODS

Detailed methods are provided in the online version of this paper and include the following:

- KEY RESOURCES TABLE
- EXPERIMENTAL MODEL AND STUDY PARTICIPANT DETAILS
  - Cell lines
  - *In vivo* models
  - Spheroids
  - Human data
- METHOD DETAILS
  - Cell culture
  - *In vivo* tumor growth analysis and ICB efficacy
  - TCGA MSI and CIBERSORT analysis
  - Spheroid growth
  - Spheroid infiltration by PBMC and ICB efficacy
  - Flow cytometry analysis
  - Bi-photon spheroid imaging
  - Whole exome sequencing (WES)
  - Single cell mRNA and TCR V(D)J sequencing
  - Visium Spatial Gene Expression analysis
- QUANTIFICATION AND STATISTICAL ANALYSIS
  - Data analysis, quantification and visualization
  - Statistics

SUPPORTING CITATIONS

The following references appear in the supplemental information:[66,67].

SUPPLEMENTAL INFORMATION

Supplemental information can be found online at https://doi.org/10.1016/j.xcrm.2026.102786.

Received: March 3, 2025
Revised: January 29, 2026
Accepted: April 8, 2026
Published: May 5, 2026

REFERENCES

1. Mestrallet, G., Brown, M., Bozkus, C.C., and Bhardwaj, N. (2023). Immune escape and resistance to immunotherapy in mismatch repair deficient tumors. Front. Immunol. *14*, 1210164.
2. Gryfe, R., Kim, H., Hsieh, E.T., Aronson, M.D., Holowaty, E.J., Bull, S.B., Redston, M., and Gallinger, S. (2000). Tumor microsatellite instability and clinical outcome in young patients with colorectal cancer. N. Engl. J. Med. *342*, 69–77. https://doi.org/10.1056/NEJM200001133420201.
3. Yamamoto, H., Perez-Piteira, J., Yoshida, T., Terada, M., Itoh, F., Imai, K., and Perucho, M. (1999). Gastric cancers of the microsatellite mutator phenotype display characteristic genetic and clinical features. Gastroenterology *116*, 1348–1357. https://doi.org/10.1016/s0016-5085(99)70499-3.
4. Cancer Genome Atlas Network (2012). Comprehensive molecular characterization of human colon and rectal cancer. Nature *487*, 330–337. https://doi.org/10.1038/nature11252.
5. Cancer Genome Atlas Research Network; Kandoth, C., Schultz, N., Cherniack, A.D., Akbani, R., Liu, Y., Shen, H., Robertson, A.G., Pashtan, I., Shen, R., et al. (2013). Integrated genomic characterization of endometrial carcinoma. Nature *497*, 67–73. https://doi.org/10.1038/nature12113.
6. Mandal, R., Samstein, R.M., Lee, K.-W., Havel, J.J., Wang, H., Krishna, C., Sabio, E.Y., Makarov, V., Kuo, F., Blecua, P., et al. (2019). Genetic diversity of tumors with mismatch repair deficiency influences anti-PD-1 immunotherapy response. Science *364*, 485–491. https://doi.org/10.1126/science.aau0447.
7. Le, D.T., Durham, J.N., Smith, K.N., Wang, H., Bartlett, B.R., Aulakh, L.K., Lu, S., Kemberling, H., Wilt, C., Luber, B.S., et al. (2017). Mismatch repair deficiency predicts response of solid tumors to PD-1 blockade. Science *357*, 409–413. https://doi.org/10.1126/science.aan6733.
8. Le, D.T., Uram, J.N., Wang, H., Bartlett, B.R., Kemberling, H., Eyring, A.D., Skora, A.D., Luber, B.S., Azad, N.S., Laheru, D., et al. (2015). PD-1 Blockade in Tumors with Mismatch-Repair Deficiency. N. Engl. J. Med. *372*, 2509–2520. https://doi.org/10.1056/NEJMoa1500596.
9. André, T., Shiu, K.-K., Kim, T.W., Jensen, B.V., Jensen, L.H., Punt, C., Smith, D., Garcia-Carbonero, R., Benavides, M., Gibbs, P., et al. (2020). Pembrolizumab in Microsatellite-Instability–High Advanced Colorectal Cancer. N. Engl. J. Med. *383*, 2207–2218. https://doi.org/10.1056/NEJMoa2017699.
10. Overman, M.J., Lonardi, S., Wong, K.Y.M., Lenz, H.-J., Gelsomino, F., Aglietta, M., Morse, M.A., Van Cutsem, E., McDermott, R., Hill, A., et al. (2018). Durable Clinical Benefit With Nivolumab Plus Ipilimumab in DNA Mismatch Repair–Deficient/Microsatellite Instability–High Metastatic Colorectal Cancer. J. Clin. Oncol. *36*, 773–779. https://doi.org/10.1200/JCO.2017.76.9901.
11. Rousseau, B., Foote, M.B., Maron, S.B., Diplas, B.H., Lu, S., Argilés, G., Cercek, A., and Diaz, L.A. (2021). The Spectrum of Benefit from Checkpoint Blockade in Hypermutated Tumors. N. Engl. J. Med. *384*, 1168–1170. https://doi.org/10.1056/NEJMc2031965.
12. Diaz, L.A., Shiu, K.-K., Kim, T.-W., Jensen, B.V., Jensen, L.H., Punt, C., Smith, D., Garcia-Carbonero, R., Benavides, M., Gibbs, P., et al. (2022). Pembrolizumab versus chemotherapy for microsatellite instability-high or mismatch repair-deficient metastatic colorectal cancer (KEYNOTE-177): final analysis of a randomised, open-label, phase 3 study. Lancet Oncol. *23*, 659–670. https://doi.org/10.1016/S1470-2045(22)00197-8.

13. Roudko, V., Bozkus, C.C., Orfanelli, T., McClain, C.B., Carr, C., O'Donnell, T., Chakraborty, L., Samstein, R., Huang, K.-L., Blank, S.V., et al. (2020). Shared Immunogenic Poly-Epitope Frameshift Mutations in Microsatellite Unstable Tumors. Cell *183*, 1634–1649.e17. https://doi.org/10.1016/j.cell.2020.11.004.

14. Chang, K., Taggart, M.W., Reyes-Uribe, L., Borras, E., Riquelme, E., Barnett, R.M., Leoni, G., San Lucas, F.A., Catanese, M.T., Mori, F., et al. (2018). Immune Profiling of Premalignant Lesions in Patients With Lynch Syndrome. JAMA Oncol. *4*, 1085–1092. https://doi.org/10.1001/jamaoncol.2018.1482.

15. Bohaumilitzky, L., Kluck, K., Hüneburg, R., Gallon, R., Nattermann, J., Kirchner, M., Kristiansen, G., Hommerding, O., Pfuderer, P.L., Wagner, L., et al. (2021). The Different Immune Profiles of Normal Colonic Mucosa in Cancer-Free Lynch Syndrome Carriers and Lynch Syndrome Colorectal Cancer Patients. Gastroenterology *162*, 907–919. https://doi.org/10.1053/j.gastro.2021.11.029.

16. Pelka, K., Hofree, M., Chen, J.H., Sarkizova, S., Pirl, J.D., Jorgji, V., Bejnood, A., Dionne, D., Ge, W.H., Xu, K.H., et al. (2021). Spatially organized multicellular immune hubs in human colorectal cancer. Cell *184*, 4734–4752.e20. https://doi.org/10.1016/j.cell.2021.08.003.

17. Li, J., Wu, C., Hu, H., Qin, G., Wu, X., Bai, F., Zhang, J., Cai, Y., Huang, Y., Wang, C., et al. (2023). Remodeling of the immune and stromal cell compartment by PD-1 blockade in mismatch repair-deficient colorectal cancer. Cancer Cell *41*, 1152–1169.e7. https://doi.org/10.1016/j.ccell.2023.04.011.

18. Grasso, C.S., Giannakis, M., Wells, D.K., Hamada, T., Mu, X.J., Quist, M., Nowak, J.A., Nishihara, R., Qian, Z.R., Inamura, K., et al. (2018). Genetic Mechanisms of Immune Evasion in Colorectal Cancer. Cancer Discov. *8*, 730–749. https://doi.org/10.1158/2159-8290.CD-17-1327.

19. Salomé, B., Sfakianos, J.P., Ranti, D., Daza, J., Bieber, C., Charap, A., Hammer, C., Banchereau, R., Farkas, A.M., Ruan, D.F., et al. (2022). NKG2A and HLA-E define an alternative immune checkpoint axis in bladder cancer. Cancer Cell *40*, 1027–1043.e9. https://doi.org/10.1016/j.ccell.2022.08.005.

20. Tsui, C., Kretschmer, L., Rapelius, S., Gabriel, S.S., Chisanga, D., Knöpper, K., Utzschneider, D.T., Nüssing, S., Liao, Y., Mason, T., et al. (2022). MYB orchestrates T cell exhaustion and response to checkpoint inhibition. Nature *609*, 354–360. https://doi.org/10.1038/s41586-022-05105-1.

21. Roumenina, L.T., Daugan, M.V., Noé, R., Petitprez, F., Vano, Y.A., Sanchez-Salas, R., Becht, E., Meilleroux, J., Clec'h, B.L., Giraldo, N.A., et al. (2019). Tumor Cells Hijack Macrophage-Produced Complement C1q to Promote Tumor Growth. Cancer Immunol. Res. *7*, 1091–1105. https://doi.org/10.1158/2326-6066.CIR-18-0891.

22. House, I.G., Savas, P., Lai, J., Chen, A.X.Y., Oliver, A.J., Teo, Z.L., Todd, K.L., Henderson, M.A., Giuffrida, L., Petley, E.V., et al. (2020). Macrophage-Derived CXCL9 and CXCL10 Are Required for Antitumor Immune Responses Following Immune Checkpoint Blockade. Clin. Cancer Res. *26*, 487–504. https://doi.org/10.1158/1078-0432.CCR-19-1868.

23. Binnewies, M., Pollack, J.L., Rudolph, J., Dash, S., Abushawish, M., Lee, T., Jahchan, N.S., Canaday, P., Lu, E., Norng, M., et al. (2021). Targeting TREM2 on tumor-associated macrophages enhances immunotherapy. Cell Rep. *37*, 109844. https://doi.org/10.1016/j.celrep.2021.109844.

24. Katzenelenbogen, Y., Sheban, F., Yalin, A., Yofe, I., Svetlichnyy, D., Jaitin, D.A., Bornstein, C., Moshe, A., Keren-Shaul, H., Cohen, M., et al. (2020). Coupled scRNA-Seq and Intracellular Protein Activity Reveal an Immunosuppressive Role of TREM2 in Cancer. Cell *182*, 872–885.e19. https://doi.org/10.1016/j.cell.2020.06.032.

25. Molgora, M., Esaulova, E., Vermi, W., Hou, J., Chen, Y., Luo, J., Brioschi, S., Bugatti, M., Omodei, A.S., Ricci, B., et al. (2020). TREM2 Modulation Remodels the Tumor Myeloid Landscape Enhancing Anti-PD-1 Immunotherapy. Cell *182*, 886–900.e17. https://doi.org/10.1016/j.cell.2020.07.013.

26. Park, M.D., Reyes-Torres, I., LeBerichel, J., Hamon, P., LaMarche, N.M., Hegde, S., Belabed, M., Troncoso, L., Grout, J.A., Magen, A., et al. (2023). TREM2 macrophages drive NK cell paucity and dysfunction in lung cancer. Nat. Immunol. *24*, 792–801. https://doi.org/10.1038/s41590-023-01475-4.

27. Cook, M.E., Jarjour, N.N., Lin, C.-C., and Edelson, B.T. (2020). The transcription factor Bhlhe40 in immunity and autoimmunity. Trends Immunol. *41*, 1023–1036. https://doi.org/10.1016/j.it.2020.09.002.

28. Zhang, L., Li, Z., Skrzypczynska, K.M., Fang, Q., Zhang, W., O'Brien, S.A., He, Y., Wang, L., Zhang, Q., Kim, A., et al. (2020). Single-Cell Analyses Inform Mechanisms of Myeloid-Targeted Therapies in Colon Cancer. Cell *181*, 442–459.e29. https://doi.org/10.1016/j.cell.2020.03.048.

29. Huffman, A.P., Lin, J.H., Kim, S.I., Byrne, K.T., and Vonderheide, R.H. (2020). CCL5 mediates CD40-driven CD4+ T cell tumor infiltration and immunity. JCI Insight *5*, e137263. https://doi.org/10.1172/jci.insight.137263.

30. Liu, Y., Lu, R., Cui, W., Pang, Y., Liu, C., Cui, L., Qian, T., Quan, L., Dai, Y., Jiao, Y., et al. (2020). High IFITM3 expression predicts adverse prognosis in acute myeloid leukemia. Cancer Gene Ther. *27*, 38–44. https://doi.org/10.1038/s41417-019-0093-y.

31. Liu, Y., Zhou, M., Wu, J., Wen, Z., Fang, Y., Lin, L., Luo, M., Sun, L., and Liao, W. (2022). Interferon-induced transmembrane protein 2 promotes epithelial-mesenchymal transition by activating transforming growth factor-β1/small mother against decapentaplegic 2 signaling in gastric cancer. Mol. Biol. Rep. *49*, 997–1006. https://doi.org/10.1007/s11033-021-06919-4.

32. Segovia, M., Russo, S., Jeldres, M., Mahmoud, Y.D., Perez, V., Duhalde, M., Charnet, P., Rousset, M., Victoria, S., Veigas, F., et al. (2019). Targeting TMEM176B Enhances Antitumor Immunity and Augments the Efficacy of Immune Checkpoint Blockers by Unleashing Inflammasome Activation. Cancer Cell *35*, 767–781.e6. https://doi.org/10.1016/j.ccell.2019.04.003.

33. Bortolomeazzi, M., Keddar, M.R., Montorsi, L., Acha-Sagredo, A., Benedetti, L., Temelkovski, D., Choi, S., Petrov, N., Todd, K., Wai, P., et al. (2021). Immunogenomics of Colorectal Cancer Response to Checkpoint Blockade: Analysis of the KEYNOTE 177 Trial and Validation Cohorts. Gastroenterology *161*, 1179–1193. https://doi.org/10.1053/j.gastro.2021.06.064.

34. Ozato, Y., Kojima, Y., Kobayashi, Y., Hisamatsu, Y., Toshima, T., Yonemura, Y., Masuda, T., Kagawa, K., Goto, Y., Utou, M., et al. (2023). Spatial and single-cell transcriptomics decipher the cellular environment containing HLA-G+ cancer cells and SPP1+ macrophages in colorectal cancer. Cell Rep. *42*, 111929. https://doi.org/10.1016/j.celrep.2022.111929.

35. Gubin, M.M., Esaulova, E., Ward, J.P., Malkova, O.N., Runci, D., Wong, P., Noguchi, T., Arthur, C.D., Meng, W., Alspach, E., et al. (2018). High-Dimensional Analysis Delineates Myeloid and Lymphoid Compartment Remodeling during Successful Immune-Checkpoint Cancer Therapy. Cell *175*, 1014–1030.e19. https://doi.org/10.1016/j.cell.2018.09.030.

36. Cuajungco, M.P., Podevin, W., Valluri, V.K., Bui, Q., Nguyen, V.H., and Taylor, K. (2012). Abnormal accumulation of human transmembrane (TMEM)-176A and 176B proteins is associated with cancer pathology. Acta Histochem. *114*, 705–712. https://doi.org/10.1016/j.acthis.2011.12.006.

37. Nebot-Bral, L., Hollebecque, A., Yurchenko, A.A., de Forceville, L., Danjou, M., Jouniaux, J.-M., Rosa, R.C.A., Pouvelle, C., Aoufouchi, S., Vuagnat, P., et al. (2022). Overcoming resistance to αPD-1 of MMR-deficient tumors with high tumor-induced neutrophils levels by combination of αCTLA-4 and αPD-1 blockers. J. Immunother. Cancer *10*, e005059. https://doi.org/10.1136/jitc-2022-005059.

38. Harrold, E.C., Foote, M.B., Rousseau, B., Walch, H., Kemel, Y., Richards, A.L., Keane, F., Cercek, A., Yaeger, R., Rathkopf, D., et al. (2023). Neoplasia risk in patients with Lynch syndrome treated with immune checkpoint blockade. Nat. Med. *29*, 2458–2463. https://doi.org/10.1038/s41591-023-02544-9.

39. Zhou, P., Shi, H., Huang, H., Sun, X., Yuan, S., Chapman, N.M., Connelly, J.P., Lim, S.A., Saravia, J., Kc, A., et al. (2023). Single-cell CRISPR screens in vivo map T cell fate regulomes in cancer. Nature *624*, 154–163. https://doi.org/10.1038/s41586-023-06733-x.

40. Overman, M.J., Gelsomino, F., Aglietta, M., Wong, M., Limon Miron, M.L., Leonard, G., García-Alfonso, P., Hill, A.G., Cubillo Gracian, A., Van Cutsem, E., et al. (2024). Nivolumab plus relatlimab in patients with previously

treated microsatellite instability-high/mismatch repair-deficient metastatic colorectal cancer: the phase II CheckMate 142 study. J. Immunother. Cancer *12*, e008689. https://doi.org/10.1136/jitc-2023-008689.

41. Chalabi, M., Verschoor, Y.L., Tan, P.B., Balduzzi, S., Van Lent, A.U., Grootscholten, C., Dokter, S., Büller, N.V., Grotenhuis, B.A., Kuhlmann, K., et al. (2024). Neoadjuvant Immunotherapy in Locally Advanced Mismatch Repair–Deficient Colon Cancer. N. Engl. J. Med. *390*, 1949–1958. https://doi.org/10.1056/NEJMoa2400634.
42. Cillo, A.R., Cardello, C., Shan, F., Karapetyan, L., Kunning, S., Sander, C., Rush, E., Karunamurthy, A., Massa, R.C., Rohatgi, A., et al. (2024). Blockade of LAG-3 and PD-1 leads to co-expression of cytotoxic and exhaustion gene modules in CD8+ T cells to promote antitumor immunity. Cell *187*, 4373–4388.e15. https://doi.org/10.1016/j.cell.2024.06.036.
43. Andrews, L.P., Butler, S.C., Cui, J., Cillo, A.R., Cardello, C., Liu, C., Brunazzi, E.A., Baessler, A., Xie, B., Kunning, S.R., et al. (2024). LAG-3 and PD-1 synergize on CD8+ T cells to drive T cell exhaustion and hinder autocrine IFN-γ-dependent anti-tumor immunity. Cell *187*, 4355–4372.e22. https://doi.org/10.1016/j.cell.2024.07.016.
44. Hirschhorn, D., Budhu, S., Kraehenbuehl, L., Gigoux, M., Schröder, D., Chow, A., Ricca, J.M., Gasmi, B., De Henau, O., Mangarin, L.M.B., et al. (2023). T cell immunotherapies engage neutrophils to eliminate tumor antigen escape variants. Cell *186*, 1432–1447.e17. https://doi.org/10.1016/j.cell.2023.03.007.
45. Blomberg, O.S., Spagnuolo, L., Garner, H., Voorwerk, L., Isaeva, O.I., van Dyk, E., Bakker, N., Chalabi, M., Klaver, C., Duijst, M., et al. (2023). IL-5-producing CD4+ T cells and eosinophils cooperate to enhance response to immune checkpoint blockade in breast cancer. Cancer Cell *41*, 106–123.e10. https://doi.org/10.1016/j.ccell.2022.11.014.
46. de Vries, N.L., van de Haar, J., Veninga, V., Chalabi, M., Ijsselsteijn, M.E., van der Ploeg, M., van den Bulk, J., Ruano, D., van den Berg, J.G., Haanen, J.B., et al. (2023). γδ T cells are effectors of immunotherapy in cancers with HLA class I defects. Nature *613*, 743–750. https://doi.org/10.1038/s41586-022-05593-1.
47. Mestrallet, G., Sone, K., and Bhardwaj, N. (2022). Strategies to overcome DC dysregulation in the tumor microenvironment. Front. Immunol. *13*, 980709.
48. Strauss, L., Mahmoud, M.A.A., Weaver, J.D., Tijaro-Ovalle, N.M., Christofides, A., Wang, Q., Pal, R., Yuan, M., Asara, J., Patsoukis, N., and Boussiotis, V.A. (2020). Targeted deletion of PD-1 in myeloid cells induces antitumor immunity. Sci. Immunol. *5*, eaay1863. https://doi.org/10.1126/sciimmunol.aay1863.
49. De Henau, O., Rausch, M., Winkler, D., Campesato, L.F., Liu, C., Cymerman, D.H., Budhu, S., Ghosh, A., Pink, M., Tchaicha, J., et al. (2016). Overcoming Resistance to Checkpoint Blockade Therapy by Targeting PI3K-γ in Myeloid Cells. Nature *539*, 443–447. https://doi.org/10.1038/nature20554.
50. Zeestraten, E.C.M., Reimers, M.S., Saadatmand, S., Goossens-Beumer, I.J., Dekker, J.W.T., Liefers, G.J., van den Elsen, P.J., van de Velde, C.J.H., and Kuppen, P.J.K. (2014). Combined analysis of HLA class I, HLA-E and HLA-G predicts prognosis in colon cancer patients. Br. J. Cancer *110*, 459–468. https://doi.org/10.1038/bjc.2013.696.
51. Garziera, M., Bidoli, E., Cecchin, E., Mini, E., Nobili, S., Lonardi, S., Buonadonna, A., Errante, D., Pella, N., D'Andrea, M., et al. (2015). HLA-G 3'UTR Polymorphisms Impact the Prognosis of Stage II-III CRC Patients in Fluoropyrimidine-Based Treatment. PLoS One *10*, e0144000. https://doi.org/10.1371/journal.pone.0144000.
52. Mestrallet, G., Auvré, F., Schenowitz, C., Carosella, E.D., LeMaoult, J., Martin, M.T., Rouas-Freiss, N., and Fortunel, N.O. (2021). Human Keratinocytes Inhibit CD4+ T-Cell Proliferation through TGFB1 Secretion and Surface Expression of HLA-G1 and PD-L1 Immune Checkpoints. Cells *10*, 1438. https://doi.org/10.3390/cells10061438.
53. Mestrallet, G., Carosella, E.D., Martin, M.T., Rouas-Freiss, N., Fortunel, N.O., and LeMaoult, J. (2022). Immunosuppressive Properties of Epidermal Keratinocytes Differ According to Their Immaturity Status. Front. Immunol. *13*, 786859.
54. Mestrallet, G., Rouas-Freiss, N., LeMaoult, J., Fortunel, N.O., and Martin, M.T. (2021). Skin Immunity and Tolerance: Focus on Epidermal Keratinocytes Expressing HLA-G. Front. Immunol. *12*, 772516.
55. Cao, M., Yie, S.-M., Liu, J., Ye, S.R., Xia, D., and Gao, E. (2011). Plasma soluble HLA-G is a potential biomarker for diagnosis of colorectal, gastric, esophageal and lung cancer. Tissue Antigens *78*, 120–128. https://doi.org/10.1111/j.1399-0039.2011.01716.x.
56. Ferretti, S., Hamon, J., de Kanter, R., Scheufler, C., Andraos-Rey, R., Barbe, S., Bechter, E., Blank, J., Bordas, V., Dammassa, E., et al. (2024). Discovery of WRN inhibitor HRO761 with synthetic lethality in MSI cancers. Nature *629*, 443–449. https://doi.org/10.1038/s41586-024-07350-y.
57. Juric, V., Mayes, E., Binnewies, M., Lee, T., Canaday, P., Pollack, J.L., Rudolph, J., Du, X., Liu, V.M., Dash, S., et al. (2023). TREM1 activation of myeloid cells promotes antitumor immunity. Sci. Transl. Med. *15*, eadd9990. https://doi.org/10.1126/scitranslmed.add9990.
58. Mestrallet, G., Ward, R.W., Brown, M., Boumelha, J., Rentzeperis, F., Vaninov, N., Saffern, M., Olumuyide, E., Suri, P., Balan, S., et al. (2025). Targeting neoantigens conserved across organs and species overcomes tumor immune escape. Preprint at bioRxiv. https://doi.org/10.1101/2025.09.25.678519.
59. Thorsson, V., Gibbs, D.L., Brown, S.D., Wolf, D., Bortone, D.S., Ou Yang, T.H., Porta-Pardo, E., Gao, G.F., Plaisier, C.L., Eddy, J.A., et al. (2018). The Immune Landscape of Cancer. Immunity *48*, 812–830.e14. https://doi.org/10.1016/j.immuni.2018.03.023.
60. Cho, N.W., Guldberg, S.M., Nabet, B.Y., Yu, J.Z., Kim, E.J., Hiam-Galvez, K.J., Yee, J.L., DeBarge, R., Tenvooren, I., Ashitey, N.A., et al. (2025). T Cells Instruct Immune Checkpoint Inhibitor Therapy Resistance in Tumors Responsive to IL1 and TNFα Inflammation. Cancer Immunol. Res. *13*, 229–244. https://doi.org/10.1158/2326-6066.CIR-24-0416.
61. Newman, A.M., Liu, C.L., Green, M.R., Gentles, A.J., Feng, W., Xu, Y., Hoang, C.D., Diehn, M., and Alizadeh, A.A. (2015). Robust enumeration of cell subsets from tissue expression profiles. Nat. Methods *12*, 453–457. https://doi.org/10.1038/nmeth.3337.
62. Guyon, J., Andrique, L., Pujol, N., Røsland, G.V., Recher, G., Bikfalvi, A., and Daubon, T. (2020). A 3D Spheroid Model for Glioblastoma. J. Vis. Exp. *158*, e60998. https://doi.org/10.3791/60998.
63. Lugand, L., Mestrallet, G., Laboureur, R., Dumont, C., Bouhidel, F., Djouadou, M., Masson-Lecomte, A., Desgrandchamps, F., Culine, S., Carosella, E.D., et al. (2022). Methods for Establishing a Renal Cell Carcinoma Tumor Spheroid Model With Immune Infiltration for Immunotherapeutic Studies. Front. Oncol. *12*, 898732.
64. Ewels, P.A., Peltzer, A., Fillinger, S., Patel, H., Alneberg, J., Wilm, A., Garcia, M.U., Di Tommaso, P., and Nahnsen, S. (2020). The nf-core framework for community-curated bioinformatics pipelines. Nat. Biotechnol. *38*, 276–278. https://doi.org/10.1038/s41587-020-0439-x.
65. Garcia, M., Juhos, S., Larsson, M., Olason, P.I., Martin, M., Eisfeldt, J., DiLorenzo, S., Sandgren, J., Ståhl, T.D.D., Ewels, P., et al. (2020). Sarek: A portable workflow for whole-genome sequencing analysis of germline and somatic variants. F1000Research *9*, 63. https://doi.org/10.12688/f1000research.16665.2.
66. Zhou, Y., Zhou, B., Pache, L., Chang, M., Khodabakhshi, A.H., Tanaseichuk, O., Benner, C., and Chanda, S.K. (2019). Metascape provides a biologist-oriented resource for the analysis of systems-level datasets. Nat. Commun. *10*, 1523. https://doi.org/10.1038/s41467-019-09234-6.
67. Mestrallet, G. (2024). Predicting Immunotherapy Outcomes in Glioblastoma Patients through Machine Learning. Cancers *16*, 408. https://doi.org/10.3390/cancers16020408.

STAR★METHODS

KEY RESOURCES TABLE

REAGENT or RESOURCE	SOURCE	IDENTIFIER
Antibodies		
anti-CD3 Rat Alexa Fluor 488	BioLegend	201406
anti-mouse CD4 [GK1.5] Alexa Fluor 532	Thermo Scientific	M001T02Y02-A
anti-mouse F4/80 [BM8] Alexa Fluor 532	eBioscience	58-480-182
anti-mouse H-2Dd [34-2-12] PE (Phycoerythrin)	BioLegend	110607
anti-CD370 (CLEC9A) Rat [7H11] PE (Phycoerythrin)	BioLegend	143505
anti-CD25 Rat [PC61] Pe/dazzle™ 594	BioLegend	102048
anti-mouse CD86 [GL-1] Pe/dazzle™ 594	BioLegend	105042
anti-CD11b Rat [M1/70] PerCP	BioLegend	101230
anti-TIGIT [GIGD7] PerCP-eFluor 710	Thermo Scientific	50-112-3954
anti-CD274 Rat [10F.9G2] PE (Phycoerythrin)/Cy7®	BioLegend	124314
anti-mouse I-A/I-E [M5/114.15.2] APC	BioLegend	107614
anti-mouse CD45 Spark NIR™ 685	BioLegend	103168
anti-mouse TCF-7/TCF-1 [S33-966] R718	BD	567587
anti-Ly-6C Rat [HK1.4] Alexa Fluor® 700	BioLegend	128002
anti-mouse FcεRIα APC/Fire™ 750	BioLegend	134340
anti-mouse CD69 [H1.2F3] APC/Cy7	BioLegend	104526
anti-mouse CD279 (PD-1) [J43] Super Bright 436	Thermo Scientific	62-9985-82
anti-mouse CD206 (MMR) [MR6F3] eFluor 450	Thermo Scientific	48-2061-82
anti-FOXP3 Rat [MF-14] Pacific Blue	BioLegend	126402
anti-CD335 Rat [29A1.4] Brilliant Violet® 510	BioLegend	137623
anti-CD103 Armenian Hamster [2E7] Brilliant Violet® 510	BioLegend	121423
anti-CD19 Rat [6D5] Brilliant Violet® 570	BioLegend	115535
anti-CD11c Armenian Hamster [N418] Brilliant Violet® 570	BioLegend	117331
anti-rat CD8a [53–6.7] Brilliant Violet® 605	BioLegend	100743
anti-mouse/human Ki-67 Brilliant Violet 650™	BioLegend	151215
anti-mouse CD117 (c-kit) Brilliant Violet 650™	BioLegend	105853
anti-mouse CD366 (Tim-3) Brilliant Violet 711™	BioLegend	134021
anti-rat Ly-6G/Ly-6C (Gr-1) [RB6-8C5] Brilliant Violet® 711	BioLegend	108443
anti-mouse Ly-6G [1A8] Brilliant Violet 785™	BioLegend	127645
anti-mouse CD223 (LAG-3) [C9B7W] Brilliant Violet 785™	BioLegend	125219
anti-human CD16 NovaFluor Blue 510	Thermo Scientific	H006T03B01-A
anti-human CD11c FITC	Biolegend	301604
anti-human FOXP3 Alexa Fluor 532	Thermo Scientific	58-4776-42
anti-human CD19 NovaFluor Blue 585	Thermo Scientific	H004T03B04-A
anti-human CD4 NovaFluor Blue 610-70S	Thermo Scientific	H001T03B06-A
anti-human CD45 PerCP Cy5.5	BD	564106
anti-human HLA-ABC PercCP-efluor 710	Thermo Scientific	46-9983-42
anti-human TIGIT BV421	BD	747844

(*Continued on next page*)

Continued

REAGENT or RESOURCE	SOURCE	IDENTIFIER
anti-human ILT2 SB436	Biolegend	62-5129-42
anti-human CD3 Pacific Blue	BD	558124
anti-human CD11b BV480	BD	746704
anti-human CD25 BV510	BD	740198
anti-human CD56 BV570	Biolegend	362540
anti-human FCER1A BV605	Biolegend	334628
anti-human CD86 BV650	Biolegend	305428
anti-human CD68 BV711	BD	565594
anti-human CD15 BV750	BD	747426
anti-human LAG3 BV786	BD	744727
anti-human TCF1 Alexa Fluor 647	Biolegend	655204
anti-human HLA-DR APC Fire 810	Biolegend	307674
anti-human HLA-G Alexa Fluor 700	Miltenyi	130-129-292
anti-human PD-1 APC Cy7	Biolegend	329922
anti-human TIM3 PE	Biolegend	345006
anti-human CD14 NovaFluor Yellow 610	Biolegend	H007T03Y03-A
anti-human CD66b PE/Fire 640	Biolegend	392918
anti-human CD117 PE Cy5	Biolegend	15-1178-42
anti-human CD8 NovaFluor Yellow 700	Biolegend	M003T02Y06-A
anti-human PD-L1 PE Cy7	BD	558017
anti-human CD1c BUV395	BD	742751
anti-human CD206 BUV737	BD	741860
anti-human CD141 BUV661	Biolegend	741650
Biological samples		
MMRd colorectal cells	This paper	N/A
CT26, B16F10, 4T1 and MC38 tumors	This paper	N/A
BALBC and BL6 spleens and lymph nodes	This paper	N/A
Deposited data		
scRNAseq	This paper	https://data.mendeley.com/datasets/ct2m5rfwvm/1
TCRseq	This paper	https://data.mendeley.com/datasets/ct2m5rfwvm/1
SpatialRNAseq	This paper	https://data.mendeley.com/datasets/ct2m5rfwvm/1
Experimental models: Cell lines		
CT26 WT	This paper	N/A
CT26 MSH2 KO	This paper	N/A
B16F10 WT	This paper	N/A
B16F10 MSH2 KO	This paper	N/A
4T1 WT	This paper	N/A
4T1 MSH2 KO	This paper	N/A
MC38	This paper	N/A
Experimental models: Organisms/strains		
BALBC *mus musculus*	Jackson Laboratories	000651
BL6 *mus musculus*	Jackson Laboratories	000664
Software and algorithms		
Python3, with Matplotlib, Scanpy, Seaborn, Scirpy, Scanpy, Squidpy, Scanorama, Pandas, SciPy and Statsmodels modules	This paper	https://github.com/gmestrallet/

EXPERIMENTAL MODEL AND STUDY PARTICIPANT DETAILS

Cell lines

CT26, 4T1 and B16F10 cells deleted for MSH2 were provided by R.Samstein[6] and N.W.Cho.[60] Guide RNA sequences (5′-CGGTGCGCCTCTTCGACCGC-3′) and (5′- GCACGGAGAGGACGCGCTGC-3′) targeting mouse Msh2 exon 1 were cloned into the PX461 plasmid and co-transfected into mouse CT26 mouse colon carcinoma cells using GenJetTM (SignaGen) *In Vitro* DNA Transfection Reagent following the manufacturer's protocol. 48 h following transfection, GFP+ cells were seeded at one cell per 96-well by the Flow Cytometry Core Facility (FCCF). Cells were grown in RPMI supplemented with 10% FBS. Single cell clones were expanded and depletion of MSH2 was confirmed by Western Blot (anti-MSH2 monoclonal antibody (FE11), Invitrogen Antibodies). Confirmed $Msh2^{-/-}$ single cell subclones were expanded and used for serial passaging and downstream *in vivo* studies further described below.

In vivo models

2 * 10 ^5 WT CT26 cells or CT26 MSH2 KO or 4T1 MSH2 KO or B16F10 MSH2 KO or MC38 cells in 100 μL of PBS were orthotopically or subcutaneously injected in 6-week old BALB/c or BL6 mice (Jackson Laboratories). The Institutional Animal Care and Use Committee (IACUC) ethic committee (IACCR202500000183/IACUC-2029-0062) approved all experiments and housing conditions for animal in this article. All groups were composed of half male and half females. Mice were maintained in a specific pathogen-free facility at the Icahn School of Medicine at Mount Sinai. Animals were housed in individually ventilated cages (5 animals per cage) and provided *ad libitum* access to food and water. All experiments were performed in accordance with protocols approved by the IACUC of the Icahn School of Medicine at Mount Sinai (IACCR202500000183/IACUC-2029-0062).

Spheroids

Murine spheroids were obtained with the cell lines described above. For patient derived-spheroids, cells were obtained from patients from the Mount Sinai Health System with evidence of a germline mutation associated with Lynch syndrome (MLH1, MSH2, MSH6, PMS2, and EPCAM) or the development of MSI-H cancer (with immunohistochemical verification of MMR protein loss) undergoing treatment or routine surveillance screening (along with MSS controls). A 72-year-old male patient with Lynch syndrome–associated MSI-H colorectal cancer who had previously received right hemicolectomy, adjuvant FOLFOX, debulking surgery with HIPEC, and adjuvant FOLFIRI provided tumor tissue for spheroid generation (sample collected February 20, 2020). Ethics approval and consent to use patient materials were obtained using our active IRB protocols (21–01317 and 19–00936).

Human data

We used raw RNAseq data from The Cancer Genome Atlas (TCGA) presented in two previous works and merged using TCGA identifiers.[13,59] A reanalysis of previously published human MMRd CRC patient data[17] has also been conducted, focusing on patients with complete or incomplete responses to anti-PD-1 therapy alone, and scrutinizing the underlying T cell and macrophage profiles. Patient information from TCGA and other previous studies are available in the original articles cited above. Patients from the Mount Sinai Health System with evidence of a germline mutation associated with Lynch syndrome (MLH1, MSH2, MSH6, PMS2, and EPCAM) or the development of MSI-H cancer (with immunohistochemical verification of MMR protein loss) undergoing treatment or routine surveillance screening (along with MSS controls) were recruited to our active IRB protocols (21–01317 and 19–00936). A 72-year-old male patient with Lynch syndrome–associated MSI-H colorectal cancer who had previously received right hemicolectomy, adjuvant FOLFOX, debulking surgery with HIPEC, and adjuvant FOLFIRI provided tumor tissue for spheroid generation (sample collected February 20, 2020).

METHOD DETAILS

Cell culture

Cells were amplified in RPMI media (Sigma) or DMEM media (Gibco) for cell culture. 10% FBS, 2 mM L-glutamine (Gibco) and 10% gentamicin were added to the medium. Medium was renewed 2 times a week. For cell amplification, cancer cells were seeded at 1,000 cells/cm2 and sub-cultured every week. All cultures were performed in plastic flasks (Biocoat, Becton-Dickinson). CT26 cells were serially passaged for continuous lengths of time under standard tissue culture conditions and were frozen under standard cell-specific freezing conditions with heat inactivated FBS and 10% DMSO cryoprotectant. Depletion of MSH2 was confirmed by Western Blot (anti-MSH2 monoclonal antibody (FE11), Invitrogen Antibodies).

In vivo tumor growth analysis and ICB efficacy

2 * 10 ^5 WT CT26 cells or CT26 MSH2 KO or 4T1 MSH2 KO or B16F10 MSH2 KO or MC38 cells in 100 μL of PBS were orthotopically or subcutaneously injected in 6-week old BALB/c or BL6 mice (Jackson Laboratories) (IACCR202500000183/IACUC-2029-0062). Mice with clinically palpable tumors (2 mm in diameter) were randomized into the following groups which received: isotype control IgG antibody, anti-mPD-1 Invivomab anti-mouse (CD279) (Bio X Cell), anti-TIM3 InVivoMab anti-mouse (CD366) (Bio X Cell), anti-mouse LAG-3 (Bio X Cell) (BE0174), anti-mouse CTLA-4 (CD152) (Bio X Cell), anti-mouse TREM2 (Leico), anti-mouse IL1B (Bio X

Cell) or anti-TIGIT [1B4], Mouse IgG1, Lambda (Absolute Antibody) treatment groups (~10 days post-injection). IgG or ICB antibodies (100μg) were administered intraperitoneally in 100 μL of PBS every 3–4 days (every 2 days for anti-TREM2, with a first injection of 200μg). Tumor volumes were measured weekly and calculated by the formula: (1/2) * (*Length*) * (*Width*)^2. 5 to 20 mice were used for each group. Mice were euthanized by carbon dioxide and the tumors were resected 28 days after tumor injection.

TCGA MSI and CIBERSORT analysis

We used raw RNAseq data from The Cancer Genome Atlas (TCGA) presented in two previous works and merged using TCGA identifiers.[13,59] Patient MSI status was assessed using the MSI sensor. Patient MSI status was considered as MSI-H for a MSIsensor threshold of 3.5. MSI-H patients of Uterine Corpus Endometrial Carcinoma (UCEC) and Colon Adenocarcinoma (COAD) cohorts were considered for CIBERSORT (cell-type identification by estimating relative subsets of RNA transcripts) analysis. The relative fraction of 22 immune cell types within the leukocyte compartment could be estimated using CIBERSORT.[61] Linear regressions between various immune parameters were performed using Python.

Spheroid growth

10,000 tumor cells were seeded in 200μL of RPMI medium in a nucleon sphera 96 well plate (Thermofisher). As an alternative, spheroids were grown using SpheroTribe (Idylle).[62] After 1 to 3 days, the circularity and the area of spheroids were measured as previously described in other systems.[63] Circularity = (4π Area)/(perimeter)^2, Roundness = 4 Area/($\pi \times$ major axis^2), with Area in μm^2. All parameters were measured using the ImageJ software.

Spheroid infiltration by PBMC and ICB efficacy

10,000 cells were seeded in 96 low attachment well plates (Nucleonsphera, Thermofisher) with RPMI medium, to form spheroids. PBMC were seeded in other 96-well culture plates (Thermofisher) and incubated at 37°C, in 5% CO2 in 200 μL RPMI medium supplemented with 20% FCS, enriched in gentamicin. 100,000 PBMCs were activated per well by IL-15 (40ng/mL) and treated or not with ICB (10μg/mL of anti-PD-1, anti-LAG3, anti-TIM3 or anti-TIGIT) for 3 days. Then, these 100,000 PBMC were added to each tumor spheroid (10,000 cells) for 3 days. Spheroids incubated with PBMC were isolated from PBMCs in suspension and dissociated using accutase (Corning Media Tech) with 3 cycles of 10 min or using MACS dissociator and a mouse tumor dissociation kit (Miltenyi). Then, PBMC, spheroids or spheroids incubated with activated PBMC were labeled with antibodies listed in Table S1 and Live Dead Blue (1uL of each antibody in 200uL of PBS). The collection was made using an Attune NxT flow cytometer (Thermofisher) or a spectral Aurora (Cytek). Data were analyzed using FlowJo software (BD biosciences). PBMC ability to infiltrate spheroids was analyzed by comparing CD45 expression on spheroids incubated with PBMC in different conditions. Tumor cell death was measured using propidium iodide (5μg/mL).

Flow cytometry analysis

Fresh tumors were resected and dissociated into single cell suspensions using a gentle MACS tissue dissociator and mouse tumor dissociation kit (Miltenyi). For analysis of cell-surface immune markers expression, cancer cells were processed as single-cell suspensions and stained for 30 min at room temperature with monoclonal antibodies. PBMC were labeled with antibodies listed in Table S1 and Live Dead Blue (1uL of each antibody in 200uL of PBS). Non-reactive antibodies of similar species and isotype, and coupled with same fluorochromes, were used as isotypic controls. Immune expression profiles were analyzed using an Attune NxT (Thermofisher) or a spectral Aurora (Cytek). Data were analyzed using FlowJo software (BD biosciences).

Bi-photon spheroid imaging

CT26 spheroids deleted for MSH2 were grown for 3 days and then co-cultured with or without immune cells for 3 more days and ICB. Splenocytes immune cells are previously labeled by Life Technologies celltracker Deep Red (Thermo Scientific). Spheroid cell nuclei are labeled with Molecular Probes NucBlue Fixed Cell ReadyProbes Reagent (Thermo Scientific). 3D Bi-photon imaging of spheroid infiltration by immune cells was performed using Olympus FVMPE-RS. Spheroid immune infiltration was followed on the (x/y) axis in the z-middle. z stack imaging of spheroid immune infiltration (top to middle of the spheroid) was also performed.

Whole exome sequencing (WES)

A sample sheet was generated to document murine sample details, including sample paths, using a format specifying murine ID, sample type (normal or tumor), lane information, and corresponding FASTQ files. The sample sheet, named "samplesheet.csv," was organized within the directory containing the associated FASTQ files. A job file, denoted as "submit_job.sh," was created to facilitate variant calling using Nextflow. This job file incorporated necessary module additions for Java (version 11.0.2) and Singularity (version 3.2.1). The Nextflow script executed the variant calling pipeline from nf-core/sarek, tailored for WES data analysis.[64,65] Input parameters included the path to the sample sheet (–input), maximum CPU allocation (–max_cpus), specification for only paired variant calling (–only_paired_variant_calling), selected variant calling tools (e.g., Strelka, Mutect2), reference genome (e.g., GRCm38), and output directory (–outdir). Nextflow was set up by installing the required modules for Java (version 11.0.2) and Singularity (version 3.2.1). The Nextflow executable was downloaded and configured in the user's home directory (~/nextflow). Verification of the Nextflow installation and version was performed to ensure proper functionality. Upon setup completion, variant calling

jobs were initiated for each sample using the provided job file (submit_job.sh). These jobs were submitted to the computing cluster for execution, with subsequent monitoring until completion. Variant annotation was conducted using Python scripting with the Varcode library. Variant Call Format (VCF) files were loaded, correcting genomic mismatches as necessary.

Single cell mRNA and TCR V(D)J sequencing

CT26 WT and MSH2 KO tumors were inoculated in BALC mice for 4 weeks as described above. Anti-PD-1 was administered twice a week after the 2 first weeks in half of the mice. Tumors were harvested after 4 weeks and dissociated into single cell suspensions.12 tumors (3 per condition) were used for single-cell RNA sequencing performed at the Human Immune Monitoring Center (HIMC) at Mount Sinai. Viability of single cells was assessed using Acridine Orange/Propidium Iodide viability staining reagent (Nexcelom), and debris-free suspensions of >75% viability were deemed suitable for the experiments. Tumor cells from individual mice were labeled with unique TotalSeqC hashtag antibodies (BioLegend) and pooled in equal proportion. scRNAseq was performed using the Chromium platform (10x Genomics) with the 5′ gene expression (5′ GEX) V2 kit, with a targeted recovery of 10,000 cells/lane. Each pool was loaded on three lanes to increase total cell yield. Gel-Beads in Emulsions (GEMs) were generated on the sample chip in the Chromium X system. Barcoded cDNA was extracted from the GEMs after Post-GEM RT-cleanup and amplified for 13 cycles. For GEX libraries, amplified cDNA was fragmented and subjected to end-repair, poly A-tailing, adapter ligation, and 10x-specific sample indexing following the manufacturer's protocol. For TCR V(D)J libraries, the cDNA was used as a template and the specific variable regions (V, D, and J regions) from each TCR locus are amplified and indexed following the manufacturer's protocol. Hashtab library was prepared per manufacturer's instructions (10x Genomics). All libraries were quantified using TapeStation (Agilent) and QuBit (ThermoFisher) analyses and were sequenced in paired end mode on a NovaSeq instrument (Illumina) targeting a depth of 20,000 reads per cell for GEX and 5,000 reads per cell for TCR and Hashtags. Raw fastq files were aligned to the mm10 reference genome (2020-A) reference genome and demultiplexed using Cell Ranger multi v7.0.1 (10x Genomics). Downstream analysis of 63,807 cells was performed using python and scanpy. All samples were preprocessed to remove genes that are expressed in less than 3 cells and to identify mitochondrial genes. Cells that have >20 mitochondrial genes were removed from the analysis. Data were normalized and highly-variable genes were identified. Principal component analysis and clustering were performed using the leiden graph-clustering method. Marker genes were identified for each cluster and a secondary clustering was performed to separate the immune cells and the cancer cells with the Wilcoxon Rank-Sum test. Gene expression was analyzed in the different conditions using scanpy. Single cell clustering was finally applied to the spatial samples using scanorama and scanpy. A RandomForestClassifier algorithm was also trained on a scRNAseq dataset,[17] n = 10 MMRd CRC patients. Accuracy = correct predictions/total number of predictions. Precision = correct predictions of a class/all positive true positive and false positive predictions. Recall (Sensitivity) = correct true positive predictions of a class/actual instances of the class. F1-score = harmonic mean of precision and recall.

Visium Spatial Gene Expression analysis

CT26 WT and MSH2 KO tumors were inoculated for 4 weeks in BALC mice as described above. Tumors were harvested after 4 weeks, and 4 tumors (2 per condition) were fixed in 4% PFA and incorporated in paraffin blocks. RNA quality was assessed using TapeStation (Agilent) and confirmed to be suitable for the assay with DV200 values >30%. Spatial Gene Expression assay was performed using Visium CytAssist platform following manufacturer's instructions (10x Genomics. Briefly, 5 μm FFPE tissue sections that were placed on a plain glass slide were deparaffinized and decrosslinked. The mouse whole transcriptome probe panel consisting of specific probes for each targeted gene was then added to the tissue. These probe pairs hybridize to their gene target and are then ligated to one another. Tissue slides and Visium CytAssist Spatial Gene Expression Slides were loaded into the Visium CytAssist instrument, where they were brought into proximity with one another. Each Visium CytAssist Slide contains about 5,000 Capture Areas (55 μm across) with barcoded spots that include oligonucleotides required to capture gene expression probes. Gene expression probes were released from the tissue upon CytAssist Enabled RNA Digestion & Tissue Removal, enabling capture by the spatially barcoded oligonucleotides present on the Visium slide surface. All the probes captured on a specific spot share a common Spatial Barcode. Libraries were generated from the probes and sequenced, and the Spatial Barcodes were used to associate the reads back to the tissue section images for spatial mapping of gene expression. Sequencing was performed on an Illumina NovaSeq sequencer with depth set at 25,000 read per capture spot. Fastq files were subsequently loaded on to Space Ranger (10x Genomics) for read alignment, spot detection, gene expression quantification and data visualization. SpatialRNAseq data were analyzed using Squidpy, Scanorama and Scanpy.

QUANTIFICATION AND STATISTICAL ANALYSIS

Data analysis, quantification and visualization

Spectral flow cytometry and RNAseq data were analyzed using Python 3 and Jupyter Notebook. Numpy and Pandas were used for array and data frame operations, and data visualization was performed using Matplotlib and Seaborn. scRNA-seq data were analyzed using Cell Ranger and Scanpy. Flow cytometry data were analyzed using FlowJo and Python 3. SpatialRNAseq data were analyzed using Squidpy, Scanorama and Scanpy. TCR-seq was analyzed using Scirpy.

Statistics

Statistical significance of the observed differences was determined using the Mann-Whitney two-sided U-test, *t* test or Linear regression. All data are presented as mean ± SEM. The difference was considered as significant when the *p* value was below 0.05. *: $p < 0.05$, **: $p < 0.01$ and ***: $p < 0.001$.